NAVAL
POSTGRADUATE
SCHOOL

MONTEREY, CALIFORNIA

THESIS

SENSITIVITY OF BOTTOM TOPOGRAPHY ON THE DYNAMICS AND SOUND SPEED STRUCTURE IN THE NORTHERN CANARY CURRENT SYSTEM

by

Alicia A. Hopkins

December 2006

Thesis Advisor:	Mary L. Batteen
Second Reader:	John A. Colosi

THIS PAGE INTENTIONALLY LEFT BLANK

REPORT DOCUMENTATION PAGE		*Form Approved OMB No. 0704-0188*

Public reporting burden for this collection of information is estimated to average 1 hour per response, including the time for reviewing instruction, searching existing data sources, gathering and maintaining the data needed, and completing and reviewing the collection of information. Send comments regarding this burden estimate or any other aspect of this collection of information, including suggestions for reducing this burden, to Washington headquarters Services, Directorate for Information Operations and Reports, 1215 Jefferson Davis Highway, Suite 1204, Arlington, VA 22202-4302, and to the Office of Management and Budget, Paperwork Reduction Project (0704-0188) Washington DC 20503.

1. AGENCY USE ONLY *(Leave blank)*	2. REPORT DATE December 2006	3. REPORT TYPE AND DATES COVERED Master's Thesis	
4. TITLE AND SUBTITLE Sensitivity of Bottom Topography on the Dynamics and Sound Speed Structure in the Northern Canary Current System		**5. FUNDING NUMBERS**	
6. AUTHOR(S) Alicia A. Hopkins			
7. PERFORMING ORGANIZATION NAME(S) AND ADDRESS(ES) Naval Postgraduate School Monterey, CA 93943-5000		**8. PERFORMING ORGANIZATION REPORT NUMBER**	
9. SPONSORING /MONITORING AGENCY NAME(S) AND ADDRESS(ES) N/A		**10. SPONSORING/MONITORING AGENCY REPORT NUMBER**	
11. SUPPLEMENTARY NOTES The views expressed in this thesis are those of the author and do not reflect the official policy or position of the Department of Defense or the U.S. Government.			
12a. DISTRIBUTION / AVAILABILITY STATEMENT Approved for public release: distribution is unlimited.		**12b. DISTRIBUTION CODE** A	

13. ABSTRACT (maximum 200 words)

The knowledge of the ocean environment, especially its littoral/coastal waters, is important for current and future naval operations. In particular, an accurate description of the mesoscale variability of the surface and subsurface currents is essential for optimizing Navy missions. This study determines that different types of topographic smoothing and the addition of a volume constraint to a sigma-coordinate model significantly influences the generation, evolution, and maintenance of not only the surface and subsurface currents, but also other features (upwelling, meanders, eddies, filaments, Mediterranean Outflow, and Meddies) in the Northern Canary Current System (NCCS). The NCCS is chosen for this study for its classical upwelling and equatorward surface current as well as the unique impact of the Mediterranean Outflow. The sound speed structure of these features is examined to establish which regions of the NCCS experience the largest changes in sound speed and the most intense gradients. This study demonstrates that features of classic littoral/coastal eastern boundary current systems, like the NCCS, have an important impact on the sound speed structure which can significantly impact Navy sonar operations.

14. SUBJECT TERMS Primitive Equation Model, Northern Canary Current System, Sigma-Level, Princeton Ocean Model (POM), Sound Speed, Eastern Boundary Current, Meddies, Eddies, Currents, Upwelling, Undercurrent, Meander, Filaments			**15. NUMBER OF PAGES** 125
			16. PRICE CODE
17. SECURITY CLASSIFICATION OF REPORT Unclassified	**18. SECURITY CLASSIFICATION OF THIS PAGE** Unclassified	**19. SECURITY CLASSIFICATION OF ABSTRACT** Unclassified	**20. LIMITATION OF ABSTRACT** UL

THIS PAGE INTENTIONALLY LEFT BLANK

SENSITIVITY OF BOTTOM TOPOGRAPHY ON THE DYNAMICS AND SOUND SPEED STRUCTURE IN THE NORTHERN CANARY CURRENT SYSTEM

Alicia A. Hopkins
Lieutenant, United States Navy
B.S., Marshall University, 1999

Submitted in partial fulfillment of the
requirements for the degree of

MASTER OF SCIENCE IN METEOROLOGY AND PHYSICAL OCEANOGRAPHY

from the

**NAVAL POSTGRADUATE SCHOOL
December 2006**

Author: Alicia A. Hopkins

Approved by: Mary L. Batteen
                Thesis Advisor

                John A. Colosi
                Second Reader

                Mary L. Batteen
                Chairman, Department of Oceanography

THIS PAGE INTENTIONALLY LEFT BLANK

ABSTRACT

The knowledge of the ocean environment, especially its littoral/coastal waters, is important for current and future naval operations. In particular, an accurate description of the mesoscale variability of the surface and subsurface currents is essential for optimizing Navy missions.

This study determines that different types of topographic smoothing and the addition of a volume constraint to a sigma-coordinate model significantly influences the generation, evolution, and maintenance of not only the surface and subsurface currents, but also other features (upwelling, meanders, eddies, filaments, Mediterranean Outflow, and Meddies) in the Northern Canary Current System (NCCS). The NCCS is chosen for this study for its classical upwelling and equatorward surface current as well as the unique impact of the Mediterranean Outflow.

The sound speed structure of these features is examined to establish which regions of the NCCS experience the largest changes in sound speed and the most intense gradients. This study demonstrates that features of classic littoral/coastal eastern boundary current systems, like the NCCS, have an important impact on the sound speed structure which can significantly impact Navy sonar operations.

THIS PAGE INTENTIONALLY LEFT BLANK

TABLE OF CONTENTS

LIST OF FIGURES

LIST OF TABLES

THIS PAGE INTENTIONALLY LEFT BLANK

ACKNOWLEDGMENTS

I would like to extend my heartfelt appreciation and indebtedness to my thesis advisor Dr. Mary Batteen, Chairman of the Department of Oceanography, Naval Postgraduate School (NPS), for her unfailing guidance and expert knowledge in the completion of this thesis. Her patience, insight, and sense of humor made this experience effortless.

This thesis would not have been possible without the wisdom and priceless assistance from CDR (Dr.) Tony Miller. I owe him a debt of gratitude for his unending expertise of MATLAB code and for his continuous patience with me.

My most sincere thanks, however, is to my husband Eric who was deployed to Afghanistan when I began my journey at NPS. He returned from Afghanistan to a new home in a new state and to a wife buried in homework and exams to study for. His afternoon and late night visits to see me in the library while I was studying and in the lab while I was running code mean the world to me. His never-ending support, encouragement, and love have given me the strength and commitment to achieve my Master's Degree.

You are right, Eric: I **can** do anything I set my mind to.

THIS PAGE INTENTIONALLY LEFT BLANK

I. INTRODUCTION

An accurate description of the mesoscale variability of surface and subsurface currents is essential for optimizing Navy missions. Understanding the mesoscale dynamics of the world's oceans is crucial to building data bases and developing operational forecasting models of the sea environment for defense-related operations.

As naval operations continue to occur in coastal and littoral/coastal regions, accurate predictions of shallow water acoustics are essential. Although the sound speed structure in the open ocean is well known, the complex dynamics of the littoral/coastal regions can complicate acoustic prediction near the coast. Identifying the influence of dynamical processes such as upwelling, eddies, filaments, and meanders on sound speed structure can provide better ocean models for acoustic predictions in littoral/coastal regions.

This study determines if different types of topographic smoothing (e.g., Gaussian and direct iterative methods) and the addition of a volume constraint to a sigma-coordinate model (in this case, the Princeton Ocean Model) can significantly influence the generation, evolution, and maintenance of currents, upwelling, meanders, eddies, filaments, Mediterranean Outflow, and Meddies in the Northern Canary Current System (NCCS). In this section, the descriptive, dynamic and modeling background of the NCCS region is reviewed.

A.   NORTHERN CANARY CURRENT SYSTEM (NCCS)

The NCCS forms the eastern limb of the subtropical gyre of the North Atlantic. Flowing equatorward off the west coasts of the Iberian Peninsula (IP) and Morocco, the NCCS contains classical features of an eastern boundary current (EBC) system, as well as regional anomalies. These features are wind-driven and are characterized by a climatologically weak (<10 cm/s), broad (~1000 km wide), cold surface flow towards the equator. The surface current flows in the direction of the prevailing winds with a poleward undercurrent below. The EBC thermocline is typically shallow (<30 m depth) and the region has high biological production due to vast regional upwelling (Parrish et al., 1983). While the NCCS contains a number of these classical features, the region also includes notable anomalies.

The Canary Current (CC) extends south along the western coasts of both the IP and northwest Africa from ~10°N to ~45°N. Like other EBCs, the NCCS is a relatively weak (~10-30 cm/s), broad (~1000 km), shallow (~500 m) surface current that flows equatorward year-round (Wooster et al., 1976; Batteen et al., 2000). Its surface waters are relatively cool due to upwelled water from the coast (Mittelstaedt, 1991).

Characteristic of EBCs, a subsurface poleward undercurrent flows below the surface CC over the continental slope and is relatively narrow (~10–40 km) and weak (~2-10 cm/s). Varying with season and latitude, the undercurrent is strongest between depths of ~100 m and ~600 m. In winter, the CC shoals to the north near Cabo da Roca and forms a second surface current commonly referred to as

2

the Iberian Current (IC) (Haynes and Barton, 1990). The IC is a relatively narrow (~25-40 km), weak (~20-30 cm/s), seasonal current found trapped near the coast against the shelf break (Fiuza, 1980; Frouin et al., 1990; Haynes and Barton, 1990) and is usually found north of Cabo da Roca but can be seen as far south as Cabo de Sao Vicente (Batteen et al., 2000).

The NCCS is unmatched amongst the subtropical eastern boundary currents of the world in that it contains the unique influence of Mediterranean Outflow (MO). After leaving the Strait of Gibraltar, the MO descends close to the continental slope in the Gulf of Cadiz as a narrow gravity current. This salty MO plume is deflected to the right due to the Coriolis acceleration (Bower et al., 1997) and dilutes, thickens, and becomes vertically differentiated into two distinct cores as it follows the northern rim of the Gulf of Cadiz (Iorga and Lozier, 1999; Bower et al., 1997). At ~7°W in the Gulf of Cadiz, the two cores exist at depths of ~600-900 m and ~1100-1200 m. Both cores continue to flow westward along the southern coast of Spain and turn poleward around Cabo de Sao Vicente (Amber and Howe, 1979; Iorga and Lozier, 1999). A third, shallower, poleward core of MO has also been traced from the Strait of Gibraltar northward to ~38.5°N off western Portugal (Amber, 1983). Additionally, climatological cyclonic circulation in the southwestern Gulf of Cadiz spreads the salty MO south to ~34°N (Iorga and Lozier, 1999).

Typical of other EBCs, the NCCS contains highly energetic mesoscale features, including jet-like surface currents, meanders, eddies and filaments (Johnson and Stevens, 2000). Satellite observations during periods of

upwelling-favorable winds have shown nearshore upwelling with several narrow filaments of cooler water extending off the coast of the IP (Fiuza and Sousa, 1989) and Cape Ghir in northwest Africa (Van Camp et al., 1991; Hagen et al., 1996). Upwelling filaments often extend ~80-150 km offshore with alongshore spacing of ~80-100 km between filaments (Haynes et al., 1993) and terminate with dipole eddy pairs (Fiuza et al., 1982; Barton, 1998).

Anticyclonic and cyclonic pairs of mesoscale eddies have been observed off the coast of the IP on the order of 100 km (Fiuza, 1984; Stammer et al., 1991). These mesoscale features have also been observed during periods of upwelling-favorable winds and are located near coastline irregularities, such as capes. These observations provide evidence that wind forcing, along with coastline irregularities, appears to be an important mechanism in the formation and continuance of many of the mesoscale features found in the NCCS (Batteen et al., 2000).

Unique to the NCCS is the generation of subsurface, anticyclonic, submesoscale eddies, called Meddies, which contribute to the maintenance of the Mid-Atlantic Salt Tongue (e.g., Armi et al., 1989). Meddies form from the complex flow of waters entering and exiting through the Straits of Gibraltar; cool North Atlantic water flows into the Mediterranean, while at the same time warmer, denser and more saline water exits beneath the incoming flow. The high-salinity water MO flowing out of the Mediterranean Sea descends to mid depths in the density-stratified ocean, continues as a narrow jet along the Iberian continental slope, and intermittently detaches large-scale eddies, called Meddies. This is an important process because it

maintains the relatively high mean salinity of a major water mass in the North Atlantic Ocean.

The primary generation region of Meddies is off Cabo da Roca and Cabo de Sao Vicente off southwest Portugal. Several different trajectories of Meddies have been observed, including a southwestward movement into the Canary Basin and westward translations south of the Azores (Richardson and Tychensky, 1998). It has been shown that bathymetry impacts the evolution of Meddies (Price and Baringer, 1994). The presence of sloping bathymetry along the continental margin, combined with the general circulation, generates a complex flow pattern along the slope regions. The degree to which the MO descends along the continental slope is sensitive to the steepness of the bottom slope it travels along. As the MO transits along the slope, Meddies can also spin off to form isolated eddies at abrupt changes in topography, e.g., as observed off Cabo de Sao Vicente (Serra et al., 2002; Bower et al., 1997).

Anticyclonic vortexes associated with Meddies form through frictional flow along the IP. Transiting along the coast of Portugal at ~2-5 cm/s, Meddies propagate to the southwest due to anticyclonic shear and interaction with the southward flow of the stronger CC. Observations reveal that Meddies can contain a core of Mediterranean waters ~200 to ~1000 m thick centered at about ~1000 m and are less stratified than the surrounding water. They are typically ~20-100 km in diameter and have temperature and salinity anomalies of approximately ~2°C and ~1 psu. This density structure supports an energetic anticyclonic rotation with peak azimuthal velocities of about ~30 cm/s and rotation periods of ~2-7 days (Armi et al., 1989; Hebert et al., 1990).

B.   PREVIOUS MODELING STUDIES

Previous modeling studies (e.g., Batteen et al., 2000) have focused on the driving mechanisms of complex mesoscale activities in the NCCS region, including upwelling, filaments, highly energetic eddies, and meanders. Martinho (2003) used the results of four numerical experiments of increasing complexity to investigate the roles of wind forcing, bottom topography and thermohaline gradients on the features of the NCCS. The results of this study showed that while wind forcing is the primary mechanism for generating classical EBC features, bottom topography and thermohaline gradients can play important roles in the generation, evolution, and maintenance of classical as well as unique features in the NCCS.

In a more recent study, Guthrie (2006) investigated the effect of currents, wind and eddies on the sound speed structure of two different EBC models, the NCCS and the Leeuwin Current System. She found that the dynamics of EBCs can lead to large changes in sound speed (5-15 m/s) and distort the vertical sound speed profile.

C. ORGANIZATION

The objective of this study builds on these previous studies. A new volume constraint and different types of bottom topography to the model are input and investigated to determine their effect on generation, evolution, and maintenance of currents, upwelling, meanders, eddies, filaments, MO, and Meddies, as well as on the sound speed structure in the NCCS. Knowledge gained from this study

will allow Navy oceanographers to better understand the complex ocean dynamics observed in EBCs and more accurately predict sound speed variability in these regions. In turn, the Navy will be better equipped to support mine and anti-submarine warfare operations in these areas.

The organization of this thesis is as follows: Chapter II describes the Princeton Ocean Model (POM) used throughout the study, including its data sets, preprocessing, and boundary conditions. In Chapter III, new numerical methods used to improve modeling capabilities of sigma coordinate bottom-following models are examined and compared.

The results of several process-oriented experiments (e.g., see Table 1) are discussed in Chapter IV. These experiments, arranged in order of increasing complexity, are as follows: Experiment 1 isolates the effect of wind-forcing. Experiment 2 examines the additional role of topography by incorporating a Gaussian type of bottom topography. Experiment 3 investigates the additional role of thermohaline forcing. Finally, Experiment 4 examines the sensitivity of the type of bottom topography used by incorporating an iterative instead of Gaussian type of bottom topography. These experiments seek to isolate phenomena in the current system that is generated by the various types of bottom topography. Lastly, the effects of these dynamic features are explored on the sound speed structure. Findings, conclusions and recommendations are presented in Chapter V.

Experiment Number	Annual Climatology	Bottom Topography
1	Horizontally Averaged	Flat
2	Horizontally Averaged	Smoothed with a 2-D Gaussian Filter Method
3	Full	Smoothed with a 2-D Gaussian Filter Method
4	Full	Smoothed with the 1-D Direct Iterative Method

Table 1.   Summary of experimental design.

II. MODEL DESCRIPTION

The sigma-coordinate Princeton Ocean Model (POM), established by Blumberg and Mellor (1983, 1987), is well recognized and widely used in numerical oceanography. The POM is a three-dimensional (3-D), sigma coordinate (terrain-following), primitive equation ocean model with a free surface. One unique feature of this model is its embedded second order turbulence scheme, which yields realistic Ekman surface and bottom boundary layer flows and effectively suppresses two-grid point noise in the model output (Mellor and Yamada, 1982).

Through the use of bottom-following sigma levels, the POM can realistically simulate processes associated with continental shelf flows and bottom boundary layer dynamics in local domains in coastal regions. Regions of complex topography, such as the NCCS, are simulated well with sigma coordinate models. POM has been used successfully to model coastal regions, where variations in bottom topography are important, and more recently, to model entire ocean basins (Ezer and Mellor, 1994, 1997).

Here the POM uses 21 vertical sigma levels which are most closely spaced near the surface and bottom. The vertical resolution is higher near the surface and the bottom in order to resolve both the surface boundary layer and the bottom boundary layer, which are important in coastal regions. To eliminate the time constraints for the vertical grid related to higher resolution near the surface, bottom and in shallow waters, an implicit vertical time differencing scheme is used.

The prognostic variables of the model are: potential temperature, salinity, density, three velocity components, surface elevation and turbulent kinetic energy (Blumberg and Mellor, 1987). The model has a split time step interval for external and internal modes. The external mode solves the equations for the vertically integrated momentum equations and also provides the sea surface and barotropic velocity components with a time step of six seconds. The internal mode solves the 3-D equations and has a time step of 180 seconds in the NCCS model.

The horizontal diffusion is a Smagorinsky formulation (Smagorinsky et al., 1965) in which the horizontal viscosity coefficients depend on the grid size, the velocity gradients and a slope parameter coefficient. Consistent with other POM studies, a value of 0.2 is assigned to this coefficient (Ezer and Mellor, 1997). This reduces unwanted diapycnal mixing over steep topography.

All choices for processes and values used in the model are the default POM parameters unless specifically described otherwise. This formulation is documented in detail by Mellor (2004).

A.   DATA SETS

The model domain (Figure 1a) encompasses the west coasts of Iberia and Morocco, extending from 30°N to 41.5°N and from 5°W to 16.5°W. The coastal boundaries of the model domain are closed, including the Strait of Gibraltar. The northern, western, and southern borders are open boundaries.

Topographic data was collected from the Institute of Geophysics and Planetary Physics, University of California

San Diego (Sandwell and Smith, 1996) from a compilation of 30 years of data soundings by ships. In vast regions, where there is sparse or no ship data, gravity estimates, derived from altimetry data, are used to interpolate soundings. The bottom topography has a horizontal of 2 minutes (1/30 of a degree).

The model is initialized using annual climatological temperature and salinity values obtained from Levitus and Boyer (1994) and Levitus et al. (1994). This data set has a one-by-one degree horizontal resolution. Climatological wind fields are obtained from the European Centre for Medium Range Weather Forecasts (ECMWF) near-surface wind analyses (Trenberth et al., 1990). The wind data is formulated on a 2.5-by-2.5 degree grid. All experiments are performed on a beta plane with a realistic coastline.

B.   PRE-PROCESSING

Pressure gradient force errors (PGFE) in a sigma coordinate model are inevitable due to sloping sigma levels. The main concern when using a terrain bottom-following ocean model is to reduce the PGFE. The highest resolution in the model domain is where the values of the slope parameter, defined as the absolute value of the ratio of the difference between two adjacent grid cell depths and their mean depth, are largest in both the latitude and longitude directions (Mellor et al., 1998). According to Mellor et al. (1998), the maximum suggested slope parameter to be used in POM sigma coordinate models is 0.2, since greater values can induce higher PGFEs. Minimizing the slope parameter is accomplished by constructing the grid

such that the closest grid spacing is located over the steepest regions of the continental slope.

Over much of the model domain, the steepest bottom gradient still had a slope parameter greater than 0.2. Therefore, the raw topography had to be smoothed in order to minimize the PGFE. Two very different linear interpolation filters used to reduce the slope parameter are discussed in Chapter III.

The annual temperature and salinity values were obtained from the World Ocean Atlas 1994 and interpolated from the one-by-one horizontal grid at standard depths to the varying horizontal resolution and 21 vertical sigma levels of the POM using a 3-D linear interpolation scheme. Due to the changes in the vertical levels for each different type of topography used, this was done separately for the three different topographies used in this study: flat, smoothed, and iterative topographies.

Daily seasonal winds were averaged over time in order to form the annual, non-weighted, average wind vector field. The wind vectors were also interpolated for the horizontal resolution of the POM with a two-dimensional (2-D) linear interpolation scheme. Since wind stress forces the model, the annual wind vectors were then used to compute the wind stress. In all experiments, annual wind forcing is used.

C. INITIALIZATION, FORCING AND BOUNDARY CONDITIONS

As discussed above, POM was initialized with annual temperature and salinity values obtained from Levitus and Boyer (1994) and Levitus et al. (1994). Since the model runs reached a quasi-equilibrium state in a relatively

short time (<26 days), zero salinity and temperature fluxes have been prescribed at the ocean surface. Experiments 1 and 2 are initialized with horizontally averaged climatology which uses the same initial temperature and salinity over the entire model domain. Initial full temperature (Figure 2) and salinity (Figure 3) climatology of the NCCS region is used in Experiments 3 and 4. Temperature and salinity decrease roughly linearly from north to south by 3°C and 0.8 psu, respectively.

The model was forced from rest with the annual ECMWF wind fields, which were interpolated for the model grid. This wind field (Figure 4) is northerly, towards the equator, along the entire domain and increases in magnitude towards the south.

Currently, no general criteria are available that state which boundary conditions are best used for a specific model. Specifying the correct open boundary conditions (BCs) is vital for achieving realistic results. These realistic results have no reflections, clamping, spurious currents or numerical alteration of the total volume of water in the model. For free-surface models, such as the POM, one important criterion is that the BCs should be transparent to the waves. In this model, a gradient BC (Chapman, 1985), which allows geostrophic flow normal to the boundary, is used for the elevation. For inflow situations, the model is forced with annual temperature and salinity values obtained from Levitus and Boyer (1994) and Levitus et al. (1994), while for outflow situations, an advection scheme is used.

For the baroclinic velocity components normal to the boundary, an explicit wave radiation scheme based on the Sommerfield radiation condition is used. For the barotropic

velocity components, a radiation condition, the Flather radiation plus Roed local solution was used. Palma and Matano (2000) revised the Flather (1976) radiation condition using the Roed and Smedstad (1984) technique, which breaks the velocity into both global and local components. This radiation condition allows wave energy to radiate across the boundary while conserving mass inside the model domain.

Even though the topography field produces a closed Strait of Gibraltar, the MO is represented as an initial condition by the annual temperature and salinity values. Since the model runs a quasi-equilibrium state, in a relatively short manner (~26 days, not shown), the ongoing addition of heat and salinity is not required to maintain the MO.

D. SOUND SPEED CALCULATION

Sound speed is a complex function of temperature, salinity, and pressure (Fofonoff and Millard, 1983). In this study, the UNESCO international algorithm (equation) is used to calculate the speed of sound in seawater. This sound speed equation is based on the equation of Chen and Millero (1977) with coefficients recalculated by Wong and Zhu (1995). This equation is far more complicated than most others in use as pressure is used as a variable while simpler forms use depth.

Note that a number of other equations have been published for calculating the sound speed in seawater based on laboratory measurements (e.g., Wilson, 1960; Del Grosso, 1974; Coppens, 1981; and Mackenzie, 1981). Each of these is

different and there is much debate over the accuracy and range of applicability of each. In particular, Dushaw et al. (1993) has shown that there is a difference of 0.6 m/s at 5000 dbar between these equations (e.g., the Del Grosso equation and the Chen and Millero equation). Since the model results in these experiments extend to 2500 m depth, the Chen and Millero equation was chosen due to its international acceptance and greater range of applicability (i.e., applicable to shallow and deep depth as opposed to only a limited range for simpler equations).

THIS PAGE INTENTIONALLY LEFT BLANK

III. MODEL IMPROVEMENTS

A.   BOTTOM TOPOGRAPHY INCORPORATION

Velocity errors induced by the pressure gradient force
are unavoidable in 3-D sigma-coordinate models, such as the
POM. PGFEs are produced when computing the horizontal
pressure gradient near steep topography in sigma-coordinate
oceanic models (Mellor et al., 1994, 1998). Significant
error is caused by the separation of the horizontal
pressure gradient term into two parts and the subsequent
cancellation of the two terms in the presence of steeply
sloping topography, which results in large truncation
errors in the transformation from z-coordinates to sigma-
coordinates (Luo et al., 2002).

The main concern when using a terrain bottom-following
ocean model is to reduce the pressure gradient force error
(PGFE). One approach used to reduce the error is to
decrease the slope parameter. Here, two interpolation
filter techniques are discussed. One method to reduce the
slope parameter is with the traditional 2-D smoothing with
Gaussian filter, provided by the POM. The other method is a
one-dimensional (1-D) robust direct iterative technique.
This method has been shown to have the unique advantage of
maintaining coastline irregularities, continental shelves,
and relative maxima such as seamounts and islands (Martinho
and Batteen, 2006).

As listed in Table 1, Experiment 1 will use flat
bottom topography with a constant depth of 2500 m. For both
Experiments 2 and 3, smoothed bottom topography will be
incorporated. The raw topography (Figure 1b) is smoothed

17

with a linear, 2-D low-pass Gaussian filter in order to decrease the pressure gradient error to the limit of 0.2 at all grid points. The new depth of each point calculated with this filter has a non-weighted average of 15-by-15 points surrounding the point. Depths greater than 2500 m are reassigned to the maximum depth of 2500 m. Land is assigned a depth of 20 m to avoid division by zero in the model. The Strait of Gibraltar is closed. Figure 1c shows the topography after the Gaussian smoothing which is used in Experiments 2 and 3.

For Experiment 4, raw topography is smoothed with an iterative, 1-D technique (Martinho and Batteen, 2006) which also satisfies the slope criterion. This is an iterative process since a change in the topography necessary to reduce the slope parameter in one direction may alter the slope parameter in the perpendicular direction to values greater than 0.2. First, the 2-D Gaussian filter is applied to the coastline to avoid altering the adjusted slope parameters. Then, the slope parameter is calculated along each grid line in one, initial direction over the domain. Any two adjacent grid points with a slope parameter greater than 0.2 is adjusted and the line recalculated. After all grid lines in the initial direction are adjusted, the topography matrix is rotated 90 degrees. Each process is repeated until the topography is adjusted for all directions (rotated 360°). After the smoothing, land is assigned a depth of 20 m and depths greater than 2500 m are reassigned to 2500 m in order to avoid division by zero in the model. Again, the Strait of Gibraltar is closed. Figure 1d shows the topography after the iterative smoothing, which is used in Experiment 4.

For comparison, 3-D plots of the raw, Gaussian, and iterative topographies for the NCCS are shown in Figures 5a, 5b and 5c, respectively. There is a recognizable difference between the Gaussian (Figure 5b) and raw topography (Figure 5a). A significant widening of the topographic features can be seen in the Gaussian smoothed topography. There is a clear deepening, or "sinking", of seamounts and islands and a significant smoothing of the coastline irregularities. For the continental slope and rise regions, there is a relatively large change in depth.

In contrast, no noticeable differences are seen between the raw (Figure 5a) and the iterative (Figure 5c) topography. The minimum depth of the seamounts is maintained which better preserves the continental shelf and rise and coastline irregularities. The iterative method only changes the topography in areas where there are relatively high slopes and shallow depths: near the upper continental slope and around seamounts. This slight widening of the most prominent seamounts is shown in Figure 5d.

B.   INCORPORATION OF A VOLUME CONSTRAINT

An advanced volume constraint (VC) based on research performed by Marchesiello et al. (2001) is introduced to the POM as a subroutine. The VC, an adaptive algorithm to the model, is based on global correction of normal barotropic velocities.

Free-surface models, such as the POM, can lose or gain water through the boundaries. According to Marchesiello et al., (2001), it is necessary to apply an artificial volume constraint to the model since the algorithm for the

barotropic velocities is non-volume conservative. In order to conserve volume, the total volume of water transported through the boundaries is calculated at every external time step. If there is a net volume outward or inward, a correction is applied at every boundary point to obtain a net change in volume equal to zero. Since the correction is always small and is applied at every open boundary condition point, there should be no marked change in the flow structures (Marchesiello et al., 2001).

To test whether the VC is an improvement to the NCCS model, two runs were made: one with a VC and one without a VC. Even by day 1 (Figures 6a and 7a), discernible differences are noted. For example, the surface flow is stronger to the south in the run without the VC (Figure 7a) compared to the run with the VC (Figure 6a). In time, the model without the VC (Figure 7b) continues to diverge from the model with the VC (Figure 6b). In particular, the model run with the VC (Figure 6b) adjusts faster and shows more realistic results, i.e., equatorward flow to the south (consistent with the wind forcing) with no spurious poleward inflow from the southern boundary of the model.

Consistent with the findings of Marchesiello et al. (2001), adding the VC improved model stability, helped avoid accumulating errors on the long term, and improved the overall performance of the open BCs in the POM. Compared to previous studies on the NCCS which had no VC (i.e., Martinho, 2001; Guthrie, 2006), this improvement of adding the VC drastically reduced the loss of the volume at the boundaries to insignificant levels throughout the model domain. As a result, the incorporation of the VC is used in all the experiments listed in Table 1 for the NCCS.

IV. RESULTS

A. EXPERIMENT ONE

In Experiment 1 (see Table 1), the model was initialized with the horizontally averaged annual climatological temperatures and salinities, which removes all thermohaline forcing. A flat bottom with a constant depth of 2500 m eliminated any topographic effects. A realistic coastline was used and the model was forced from annually climatological winds. Using these initial conditions, the model was run for 90 days.

1. Surface Currents and Upwelling

By day 30 (Figure 8a), as expected, there is an equatorward surface current along the entire coastal region, with stronger surface currents found in the region between Cape Bedouzza and Cape Ghir (see Figure 1a for geographical locations). The stronger winds at the southward end of the model cause cooler temperatures associated with relatively strong upwelling along the entire coastline. By day 45 (Figure 8b), the offshore extent of the coastal upwelled waters has increased, particularly off the coast of Cape Ghir, where the wind stress is initially stronger. By day 75 (Figure 8d), the coldest waters are found off Cape Ghir and Cabo da Roca, and the upwelling extent continues to broaden along the entire coastline. This continuing westward propagation of upwelled water with time is consistent with the results of McCreary et al. (1987) and Batteen et al. (1989). They showed that, due to the beta effect, the surface coastal

jet does not necessarily have to be confined to within a Rossby radius of deformation of the coast.

2. Undercurrent

Below the surface, a poleward undercurrent appears by day 30 (not shown) in the opposite direction of the surface flow. A cross-section of meridional velocity at 37.4°N on day 39 (Figure 8e) shows the core of the poleward undercurrent at ~500 m depth with a speed of ~10 cm/s underlying the equatorward surface current which has a speed of ~20 cm/s. The undercurrent reaches its maximum intensity by day 45 (not shown), after which eddies and Meddies begin to form and spin off.

3. Filaments and Eddies

The upwelling-favorable equatorward winds cause cooling of the coastal waters along the coast and produces offshore flowing filaments that transport cold water into the sea interior. At the surface, several filaments of cooler water are generated from upwelling. By day 30, there is evidence of filament activity off Cabo da Roca, Cabo de Sao Vicente and Cape Ghir (Figure 8a). The coastal irregularities (i.e., capes) off these three coastal regions cause surface eddies to spin off from the filaments by day 45 (Figure 8b). By day 60, the formation of some smaller mesoscale features in the Gulf of Cadiz is also noticeable (Figure 8c). By day 75, surface eddies appear along the entire coastal domain (Figure 8d), with more developed features near coastline irregularities, including off Cabo da Roca, Cabo de Sao Vicente, Cape Beddouzza and Cape Ghir.

4. Meddies

At day 60, the development of several subsurface anticyclonic eddies off Cape Bedouzza, Cabo de Sao Vicente

and Cabo da Roca can be seen at ~1250 m depth (Figure 8f). A cross section of salinity at 39.3°N off Cabo da Roca (Figure 8g) shows a salty core with a salinity maximum of ~35.9 psu at 1250 m depth, which is consistent with the MO signature. It has been suggested (Kase et al., 1989) that Meddies are generated by the instability of the equatorward coastal jet and poleward undercurrent. The deep origin, salty signature, and anticyclonic rotation of the eddy west of Cabo de Sao Vicente are consistent with Meddy observations in this region (Richardson and Tychensky, 1998). The Meddy observed off Cabo da Roca (Figure 8f) is consistent with results of Kase et al., (1989), who observed eddies in the MO off northern Iberia.

B.   EXPERIMENT TWO

In Experiment 2, instead of a flat bottom, the Gaussian smoothed bottom topography, described in Chapter II, was added with the same model forcing conditions (see Table 1). In particular, the model was initialized with the horizontally averaged annual climatological temperatures and salinities. A realistic coastline was used along with forcing by the annual climatological winds.

1.   Surface Currents and Upwelling

In this experiment, the surface current velocities are maintained over the shelf rather than close to the shore as in the flat bottom case (e.g., compare Figures 8 and 9). The velocities also have the highest magnitudes over the continental shelf break, as indicated by the 200 m contour in Figure 9.

A comparison of the surface temperatures indicates cooler upwelled water along the entire coastline in

Experiment 2 compared to the flat bottom experiment. However, the extent of these upwelled waters in Experiment 2 is more restricted than in Experiment 1, particularly off Cape Ghir. This can be explained by the presence of bottom topography which traps the flow and opposes the tendency for westward propagation due to the planetary beta effect. Another area of stronger upwelling is near Figueira da Foz, where colder surface temperatures are present farther offshore in Experiment 2 than in Experiment 1 (e.g., compare Figures 8 and 9). This can be explained as follows: At 40.3°N, the 200 m contour depicts a prominent subsurface topographic feature which is not present in the flat bottom experiment.

2. Undercurrent

A poleward undercurrent north of the Gulf of Cadiz develops much later in Experiment 2 than in Experiment 1. Instead of forming by day 15 as in Experiment 1, the core does not form until ~day 33 (not shown). It reaches its maximum intensity by day 45. The core is also deeper in Experiment 2 than in Experiment 1 (e.g., compare Figures 8e and 9e). In Experiment 2, the core of the undercurrent is below ~1000 m depth while in Experiment 1 it is shallower below ~500 m depth. This is a likely cause for a decrease of mesoscale activity in Experiment 2. The deeper undercurrent can result in weaker vertical and horizontal shears which subsequently reduces the baroclinic and barotropic instabilities responsible for the generation of mesoscale features (Batteen, 1997; Roed and Shi, 1999). The presence of a linearly sloping bottom at the continental slope can also produce barotropic shear waves which have been demonstrated to be more stable than those found in flat bottom cases (Gawarkiewicz, 1991).

3. Filaments and Eddies

Unlike Experiment 1, which had extensive meanders and filaments (e.g., Figure 8c), the only evidence of mesoscale phenomena in Experiment 2 is a relatively strong eddy off Cabo da Roca by day 45 (Figure 9b) and another weaker eddy off Figueira da Foz (Figure 9d) by day 75. Again, the eddy off Figueira da Foz, which was not seen in Experiment 1, is associated with the topographic feature off the almost straight coastline. The filament off Cape Ghir in Experiment 1 (Figure 8c) is not present in Experiment 2 (Figure 9c). This is likely due to trapping of the surface currents by the topography which opposes the westward propagation of the upwelled waters. The presence of these features demonstrates that bottom topography plays an important role in the development and intensification of filaments.

4. Meddies

Meddy formation occurs in Experiment 2 off Cabo da Roca and off Figueira da Foz (Figure 9f). However, unlike Experiment 1, no Meddy forms in Experiment 2 off Cabo de Sao Vicente (e.g., compare Figures 8f and 9f). Note that the current follows the smoothed continental shelf in Experiment 2 rather than the coastline. In Experiment 2, this Gaussian smoothed bottom topography off the capes results in the following: Both vortex stretching and the increased radius of curvature (compared to the radius in Experiment 1) in the Gaussian smoothed topography impede the separation of the boundary current. (Note that boundary current separation is necessary for the formation of Meddies (Martinho, 2003)). As a result, no Meddy forms off Cabo de Sao Vicente in Experiment 2. In contrast, off Cabo da Roca, there is no significant change in the radius of

25

curvature from Experiment 1 to Experiment 2 (e.g., compare Figures 8f and 9f). Therefore, Meddies do occur in this location for both the flat bottom (Experiment 1) and the topography (Experiment 2) cases.

C.   EXPERIMENT THREE

Experiment 3 uses the same Gaussian smoothed bottom topography as in Experiment 2. However, this experiment uses the full annual temperature and salinity climatology, which models the observed density/sea height gradient and introduces thermohaline forcing into the model. The same forcing by annual climatological winds and a realistic coastline was used.

1.   Surface Currents and Upwelling

The equatorward surface current in Experiment 3 is comparable to that in Experiment 2 (e.g., compare Figures 9 and 10). The coastal current is slightly weaker in Experiment 3 due to the thermohaline forcing which opposes the wind forcing. Geostrophic adjustment can produce a velocity smaller in magnitude but in opposition to the main flow which reduces the current speed.

The difference in the coastal area temperatures in Experiments 2 and 3 reflect the different climatologies used in the model. For example, to the north of Figueira da Foz, there are differences in both the temperatures and the upwelling extent (e.g., compare Firgures 9a and 10b).

2.   Undercurrent

A comparison of cross-sections of the meridional velocities for Experiments 2 and 3 (Figures 9e and 10f) shows a shallower extent of the undercurrent in Experiment 3, but with a well defined core of similar magnitude at

~1000 m depth. As in Experiment 2, the deep location of the undercurrent results in weaker vertical and horizontal shears. This reduces the baroclinic and barotropic instabilities that generate mesoscale features.

3. Filaments and Eddies

In Experiment 3, broad filaments (e.g., Figure 10b) occur to the north off Cabo da Roca. A meander present off Cabo da Roca in Experiment 3 (e.g., Figure 10c) is comparable to that in Experiment 2, except that the intensity of the surface eddy offshore of the filament is much less than in Experiment 2 (e.g., compare Figures 9c and 10d). Due to the effect of full climatology used, which tightens the surface current near the coast, the extent of the filament off Cape Ghir is also less in Experiment 3 (e.g., compare Figures 9d and 10e). In Experiment 3, no surface eddy spins off Figueira da Foz as was observed in Experiment 2 (e.g., compare Figures 9d and 10e).

4. Iberian Current

In Experiment 3, thermohaline forcing was the only addition incorporated. A new feature in Experiment 3 is the formation of a poleward flow north of ~39°N (centered at ~10°W) offshore of the coastal equatorward flow which is discernible by day 5 (Figure 10a). This is consistent with the IC, which flows off the IP.

Other models have produced a similar poleward flow such as Figure 15 of Coelho et al. (2002), which is shown as Figure 11. A comparison of Figures 10a and 11 reveals that both model runs have an equatorward surface current nearshore and an offshore poleward current between ~39°N and ~42°N centered at ~10°W. Coelho et al. (2002) suggested a number of explanations for the surface poleward flow including: the type of wind forcing used (i.e.,

climatological versus actual (in their case, 1994) winds); remnant of a winter surface poleward current (generated by thermohaline forcing); and wind stress curl. In Experiment 2, no surface poleward flow was generated in this region. As a result, we conclude that of all the proposed mechanisms by Coelho et al., (2002), the surface poleward flow is likely generated by the additional thermohaline forcing instead of either by wind forcing or wind stress curl.

5. Meddies

Meddy formation occurs in Experiment 3 first off Cabo da Roca and then off Figueira da Foz (Figures 10g and 10h). As in Experiment 2, no Meddy forms off Cabo de Sao Vicente.

A comparison of the results of all three experiments shows that while most features are simulated in all the experiments, unexpectedly a realistic subsurface mesoscale feature (i.e., a Meddy off Cabo de Sao Vicente) only occurs in the flat bottom NCCS model (Experiment 1). In the next section, we will investigate if this is a consequence of the type of smoothed bottom topography used in both Experiments 2 and 3.

D. EXPERIMENT FOUR

Instead of Gaussian smoothed bottom topography, direct iterative topography, described earlier, is used in this Experiment. Note that in the direct iterative smoothing method, the continental shelf more closely approximates the raw topography than the Gaussian smoothing method (e.g., compare Figures 1b-1d and also the 200 m isobath in Figures 10 and 12). The same model forcing conditions (see Table 1)

are used as in Experiment 3. Specifically, the model is initialized with the full annual climatological temperatures and salinities and annual wind forcing.

1. Surface Currents and Upwelling

By day 5, a weak IC develops north of 39°N but is not subsequently maintained (likely due to the incorporation of annual rather than winter thermohaline forcing). By day 30, an equatorward surface current develops along the continental shelf break and upper continental slope (Figure 12b). Strong upwelling also occurs off the west coast of Morocco due to strong equatorward winds in this region. By day 45 (Figure 12c), upwelling is enhanced near the capes off the IP. By day 60, upwelling generally has a greater westward extent in Experiment 4 than in Experiment 3 (e.g., compare Figures 10d and 12d). By day 75 (Figure 12e), the offshore extent of upwelled water off Cabo da Roca and Figueira da Foz extend well seaward of the continental shelf break.

2. Undercurrent

In Figure 12f, the results for day 39 of the meridional velocity are shown in a cross-section for Experiment 4. Here, the poleward undercurrent is more confined to the slope than in Experiment 3 (e.g., compare Figures 10f and 12f). The core of the poleward undercurrent is located at ~800 m depth in Experiment 4 rather than at ~1000 m depth in Experiment 3. This shallower core of the undercurrent increases the vertical and horizontal shears and is likely responsible for the generation of greater mesoscale activity off Cabo de Sao Vicente (e.g., compare Figures 10e and 12e).

3. Filaments and Surface Eddies

In the previous Gaussian topography experiment, a weak filament developed off Cape Ghir by day 75 (Figure 12e). In Experiment 4, a filament develops off Cape Ghir much earlier, i.e., by day 30 (Figure 12b), and subsequently spins off a surface eddy (day 45, Figure 12c). A filament not found in Experiment 3 off Cabo de Sao Vicente is now present in Experiment 4 (e.g., compare Figures 10e and 12e). In particular, a surface eddy develops to the south of Cabo de Sao Vicente in the Gulf of Cadiz. While filaments extend offshore from both Cabo da Roca and Figueira da Foz at the same extent as Experiment 3 by day 45 (e.g., compare Figures 10c and 12c), a surface eddy does not spin off Cabo da Roca (i.e., by day 75, Figure 12e, compared to day 60, Figure 10d). Another feature not found in Experiment 3 but now found in Experiment 4 is surface eddy activity in the Gulf of Cadiz (e.g., compare Figures 10e and 12e).

4. Meddies

A Meddy develops to the west of Cabo de Sao Vicente by day 30 (Figure 12g), which is consistent with available observations of Meddies (e.g., Batteen et al., 2000). This Meddy was also produced in the flat bottom case (e.g., Figure 8f), but not in both Gaussian smoothed topography cases, Experiments 2 and 3 (e.g., Figures 9f and 10g). Just as in Experiment 2, a Meddy forms off Figueira da Foz (not shown), although much weaker in intensity (compare Figures 10g and 12e). As in previous experiments, a Meddy off Cabo da Roca forms (e.g., Figure 12e) and subsequently propagates to the west (not shown).

V.   EFFECTS OF NORTHERN CANARY CURRENT SYSTEM FEATURES ON SOUND SPEED STRUCTURE

A.   INTRODUCTION

The model experiments in the previous chapter reproduced the major characteristics and unique features of the NCCS and highlighted the observed mesoscale variability in the NCCS. This section demonstrates that these features lead to considerable variability in sound speed which can have a significant impact on sound speed structure.

The sound speed structure in a region is affected by two general processes: vertical displacement of ocean layers and horizontal advection of water masses (Lurton, 2002). Ocean layers are displaced vertically by features such as internal waves, and surface and subsurface eddies, which create variations in water density with depth. Upwelling, the lifting of deep water masses to the upper ocean, also vertically displaces water. Horizontal advection occurs when meanders and filaments in the surface current carry warmer water seaward, transporting large volumes of warm water.

Applying this to the NCCS region, we note that the NCCS is affected by upwelling along the coast which displaces water vertically. On the horizontal scale, the Canary Current advects cool fresh water equatorward while the undercurrent advects warm saline water poleward. There also is the advection of MO by the undercurrent which is unique to the NCCS region. Filaments can carry cooler water offshore, while eddies that detach from the current near the capes can transport large volumes of cool water. In addition, all of these processes that change the sound

speed are variable in time (as shown in Chapter IV) which can further complicate the acoustic picture.

In this chapter, we examine the sound speed structure. In particular, sound speed is calculated and plotted for horizontal levels, such as the surface. Sound speed and sound speed change are also calculated and plotted in vertical cross sections. These are used to determine how MO, upwelling, undercurrents, filaments, surface eddies and Meddies change the sound speed. Sound speed is calculated at the time of analysis and the change of sound speed is the difference in sound speed from the initial time (climatology) to the analysis time.

B.   FEATURES

1.   Mediterranean Outflow (MO)

MO is generally found throughout the NCCS model domain. For example, a cross-section of salinity through the Gulf of Cadiz at 36°N (Figure 13a) shows the MO signature centered at ~1200 m depth and also the characteristically high salinity values of the North Atlantic waters in the upper 300 m depth. To the south (32°N, Figure 13b) and to the north (39°N, Figure 13c), evidence of MO centered at ~1200 m depth can also be seen.

For the same day and latitudes, the MO signature is discernible in the sound speed profiles (Figures 13d, 13e, and 13f) creating two distinct sound channels centered at ~500 m and ~2000 m depths. This particular profile is unique to the NCCS region due to warm, salty waters of the Mediterranean mixing with the North Atlantic. Important acoustically, the double minimum features are strong not only in the Gulf of Cadiz (Figure 13d) but also towards the

south (Figure 13e) and north (Figure 13f), exemplifying the same spreading of the MO seen in salinity cross sections (Figures 13a, 13b and 13c).

2. Upwelling

In Experiment 4, a band of upwelled water is visible along the shore at the surface (Figure 12e). As expected, the surface sound speed closely resembles the temperature plot with the slowest sound speeds in areas where the temperatures are lower (e.g., compare Figures 12e and 14a). For example, a cross-section at 33.5°N (Figure 14b) shows that the upward sloping isotherms over the shelf are consistent with the presence of upwelling. There is also an upward slope in sound speed with the slower speeds in the areas of cooler waters (Figure 14c). The significantly cooler upwelled water subsequently results in a decrease of ~25 m/s in sound speed from the surface to ~500 m depth near the shelf (Figure 14d).

In the region of upwelling, sound speed fluctuation is driven by the change in temperature. Although upwelling primarily impacts the mixed layer, the horizontal gradient of sound speed in the upper layer is not widespread and changes ~25 m/s over a ~150 km distance.

3. Filaments and Surface Eddies

Several eddies of cooler water are generated on the surface. In particular, by day 75 in Experiment 4 (Figure 12e), a well-defined, cold-core eddy centered at ~11°W has spun off from these filaments at Cape Ghir. The surface sound speed is lower in the eddy than in the surrounding waters (Figure 14a). The lower sound speed in the eddy can extend to over 200 m depth. The decrease in sound speed from initial time is ~20 m/s across a ~200 km horizontal

33

distance (Figure 14d). Note that the sound speed decrease is lowest in the core of the eddy.

These mesoscale surface eddies are significant acoustical features due to their large gradients of sound speed. The sound speed structure in the eddy changes over a relatively short longitudinal distance, leading to relatively large gradients.

4.   Meddies

Meddies developed in all the experiments off Cabo de Roca. A typical cross-section of salinity shows that the core of the Meddy (e.g., Figure 15a) is salty which corresponds to a higher sound speed (Figure 15b). At 39.7°N off Cabo da Roca, a cross-section of sound speed change (Figure 15c) shows that the salty core at 1250 m depth (Figure 15d) increases the sound speed. In particular, the sound speed across the Meddy increases by ~6 m/s over a ~100 km horizontal and ~1000 m vertical region (Figure 15c). Whereas temperature is a foremost factor affecting sound speed, the NCCS represents a region uniquely affected by the highly saline MO.

5.   Undercurrent

The undercurrent (e.g., Figure 10f) advects subtropical water poleward along the western coasts. North of the Gulf of Cadiz, the undercurrent advects MO waters and has a significant effect on sound speed structure. For example, at 37.4°N (Figure 16a), the downward sloping isotherms near the shelf at ~1000 m depth and below are consistent with downwelling (Figure 16a) in conjunction with the subsurface advection of subtropical water. A cross section of sound speed difference at 37.4°N (Figure 16b) shows a ~6 m/s increase due the added salinity of the MO to

34

the warm undercurrent. This increase in sound speed occurs over a ~50 km horizontal and a ~500 m vertical extent.

THIS PAGE INTENTIONALLY LEFT BLANK

VI. SUMMARY

Several process-oriented experiments were conducted to determine if different types of topographic smoothing, e.g., Gaussian and direct iterative methods, could significantly influence the generation, evolution, and maintenance of the classical as well as unique features of the NCCS. The incorporation of a volume constraint to the terrain-following numerical ocean model, in this case the POM, was shown to improve model stability and the overall performance on the long term.

While most of the NCCS features were realistically simulated, a key comparison of the results showed that unexpectedly a realistic subsurface mesoscale feature (i.e. a Meddy off Cabo de Sao Vicente) was simulated in both the flat bottom and iterative bottom topography NCCS models but not in the model using Gaussian bottom topography. The iterative bottom topography was shown to better preserve the raw topography and subsequently produced the subsurface feature. The results of these process-oriented experiments emphasize that numerical models of ocean circulation require important choices, which are both numerical and physical.

The effects of these mesoscale features in the current system on the acoustic structure in the region were systematically examined. Recall in section V.B.1 that to the north of the Gulf of Cadiz, the added salinity of the MO caused a significant increase in sound speed (e.g., compare Figure 13 a-c to Figures 13d-f).

Table 2 summarizes the other effects of sound speed of each feature discussed in the previous section (i.e.,

37

Chapter V) for this region. Results are presented in terms of effective change in sound speed from initial conditions as well as spatial extent. Of critical acoustic importance are the spatial gradients of sound speed caused by these features.

NCCS Feature	Δc	L_x	L_z
Upwelling	-25 m/s	150 km	500 m
Surface Eddies	-20 m/s	200 km	200 m
Meddies	+6 m/s	50 km	1000 m
Undercurrent	+6 m/s	50 km	500 m

Table 2. Impact of features on sound in the NCCS.

In the NCCS, upwelling clearly experiences the greatest change on sound speed, affecting a large surface area through the mixed layer. Surface eddies which spin off upwelling filaments also cause a relatively large decrease in sound speed. The Meddies and undercurrent presented the most intense horizontal and vertical gradients of sound speed change.

Overall, this study demonstrates that features of classic coastal/littoral eastern boundary current systems, like the NCCS, do have a significant impact on the sound speed structure. Knowledge gained from this study should

allow Navy Oceanographers to better understand the complex ocean dynamics observed in the littoral/coastal systems and more accurately predict sound speed variability in these regions. In turn, the Navy will be better equipped to support mine and anti-submarine warfare operations in these areas.

THIS PAGE INTENTIONALLY LEFT BLANK

APPENDIX

This appendix contains all figures referred to throughout the text.
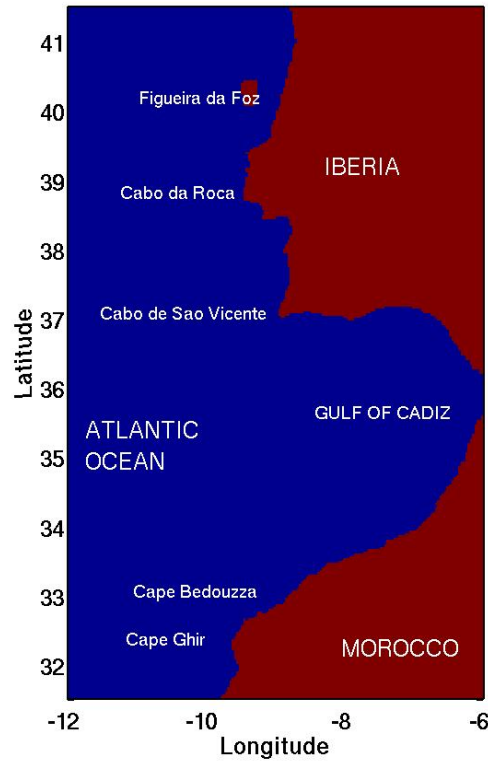
Figure 1a. Model domain for the Northern Canary Current System (NCCS) is bounded by 31.5°N to 41.5°N, 16.5°W (not shown) to 6°W. Geographical locations are labeled.
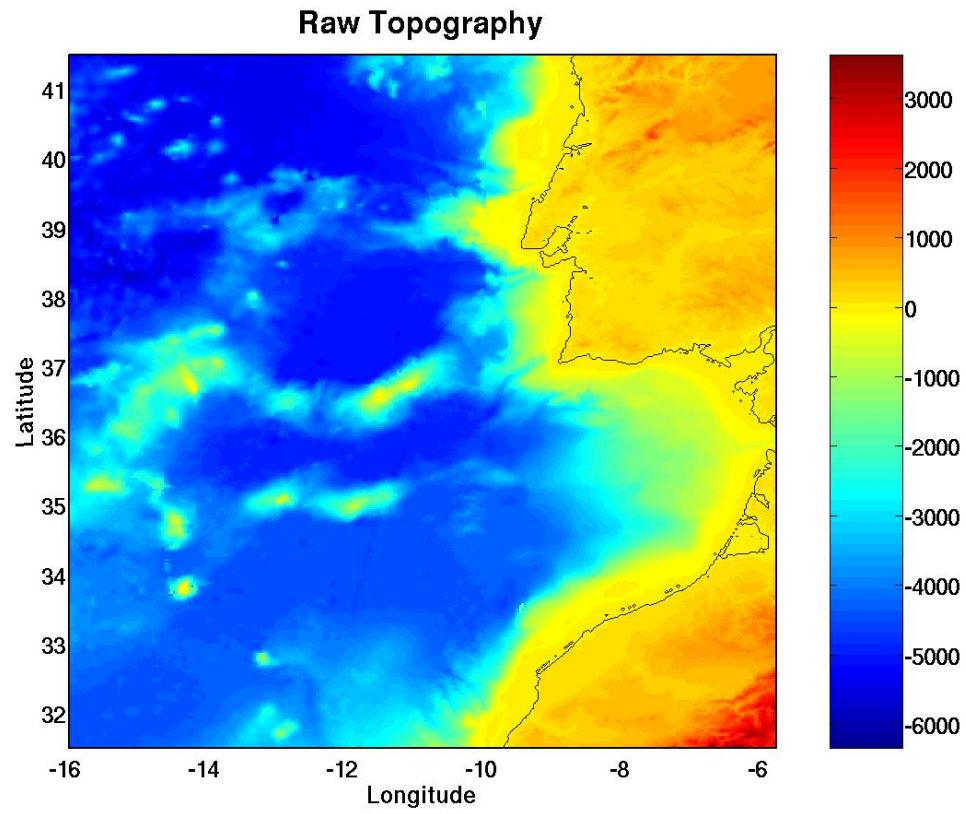
Raw Topography

Figure 1b. Raw topography, depths in m, obtained from Sandwell and Smith (1996).

Gaussian Topography
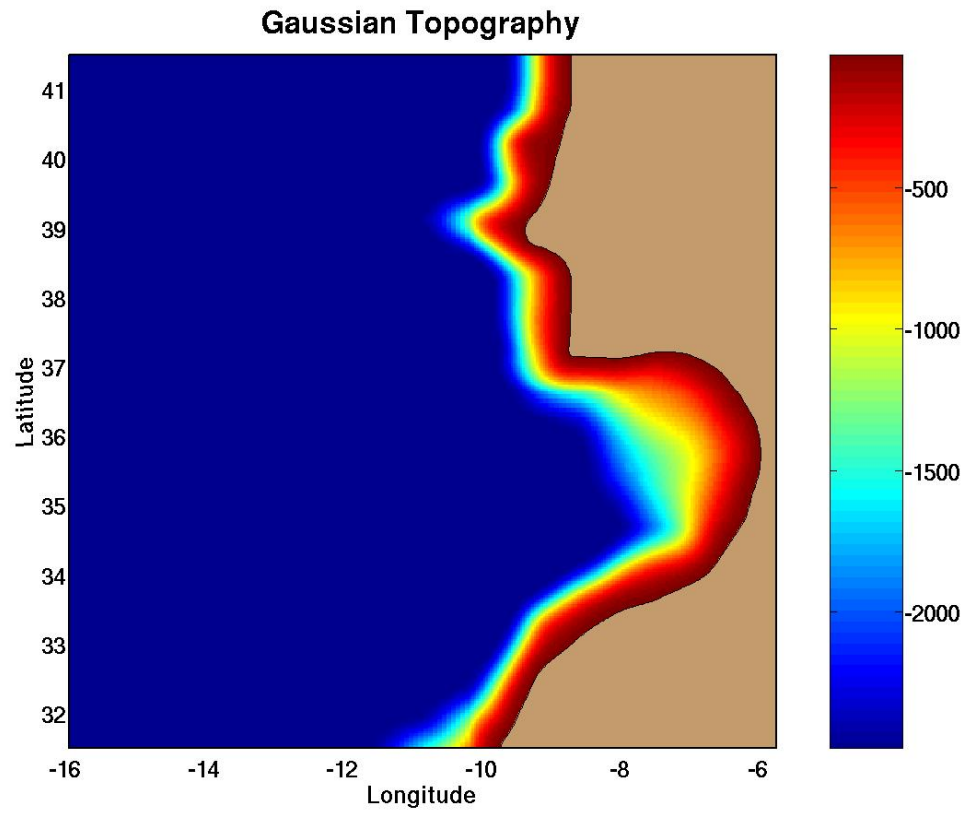
Figure 1c. Smoothed topography, depths in m, obtained from Sandwell and Smith (1996) after applying a linear two-dimensional low-pass filter.

Iterative Topography
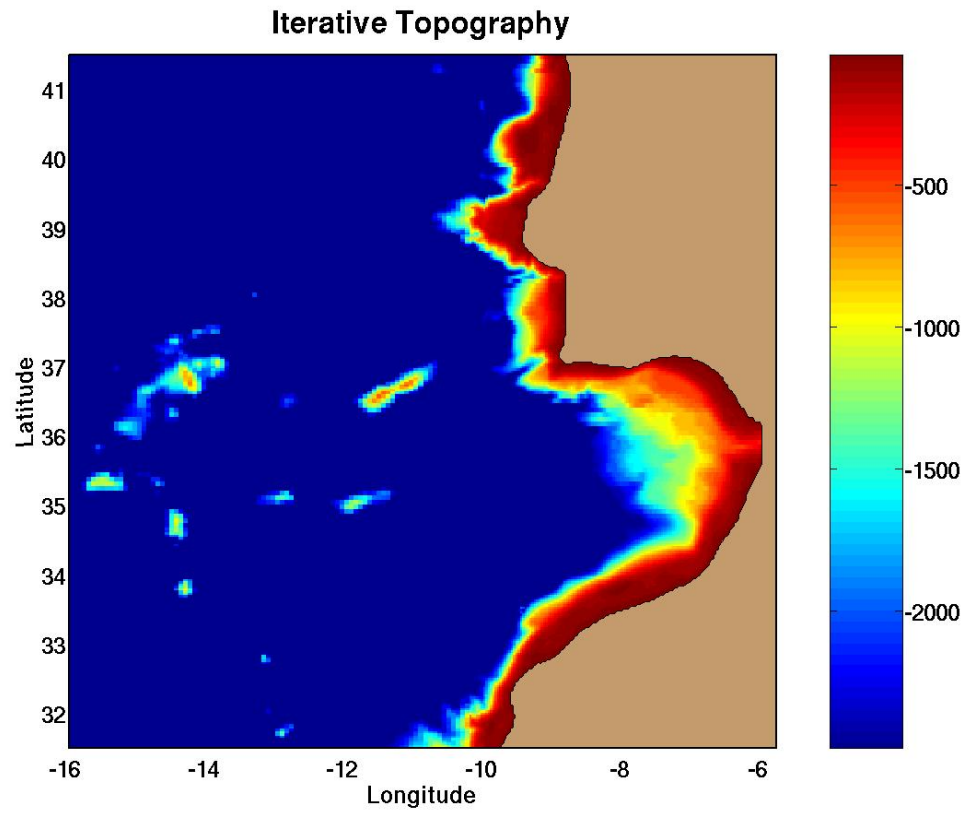
Figure 1d. Iterative topography, depths in m, obtained from Sandwell and Smith (1996) after applying a linear one-dimensional low-pass filter.
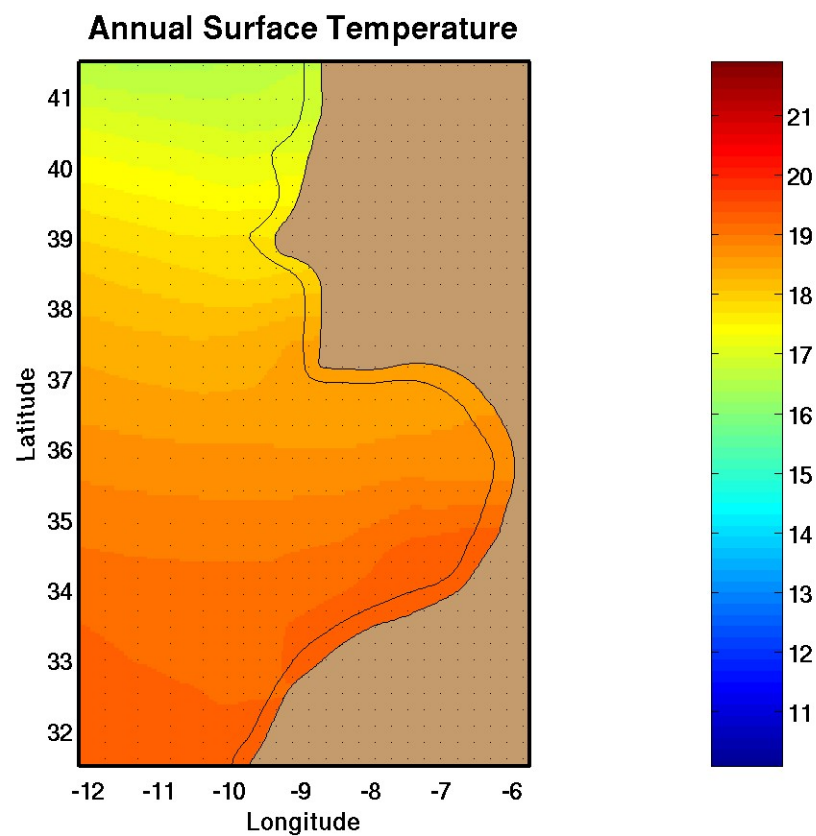
Figure 2. Levitus annual climatological surface temperature (°C).

Annual Surface Salinity
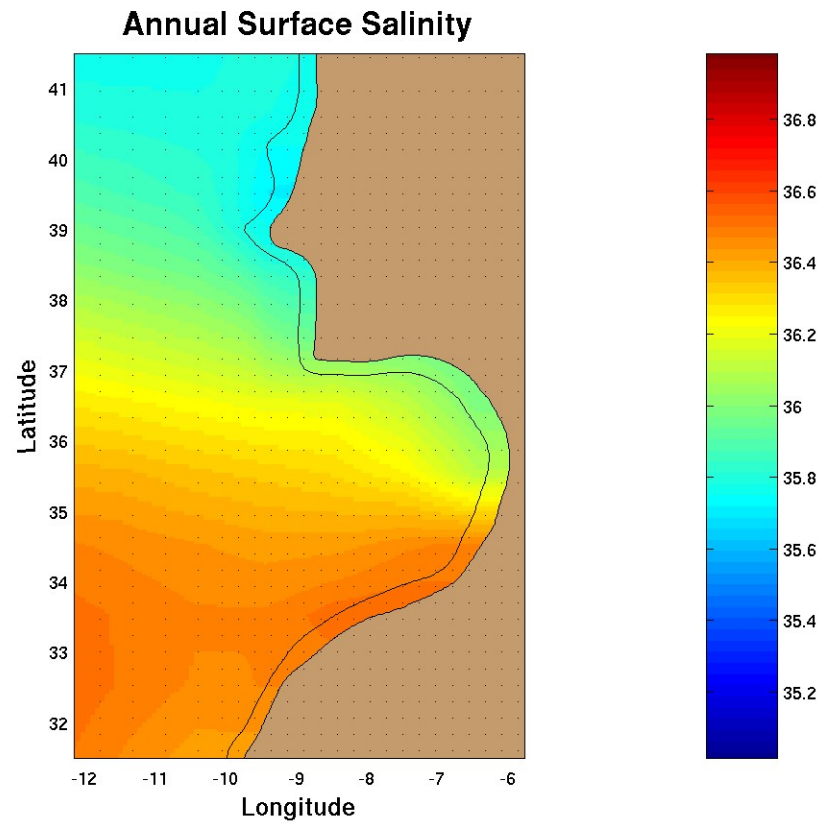
Figure 3. Levitus annual climatological surface salinity (°C).

Annual Wind Forcing
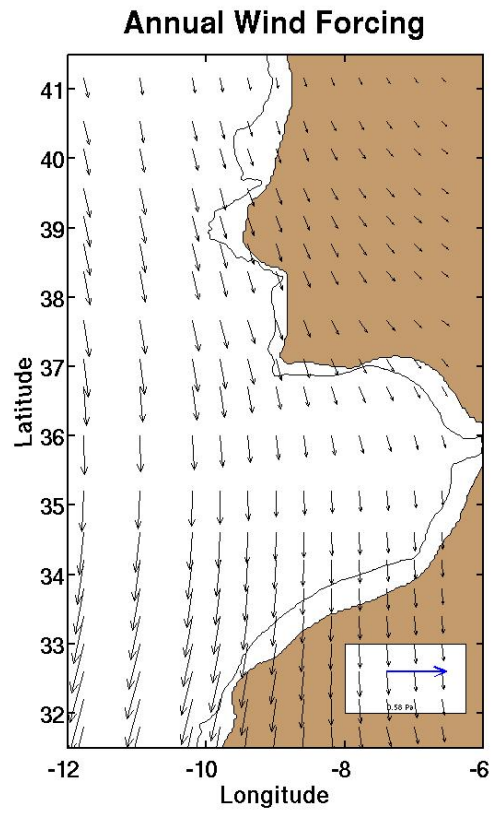
Figure 4. NCCS wind stress vectors (Pascals) calculated from annual climatological ECMWF winds (From: Trenberth et al., 1990)
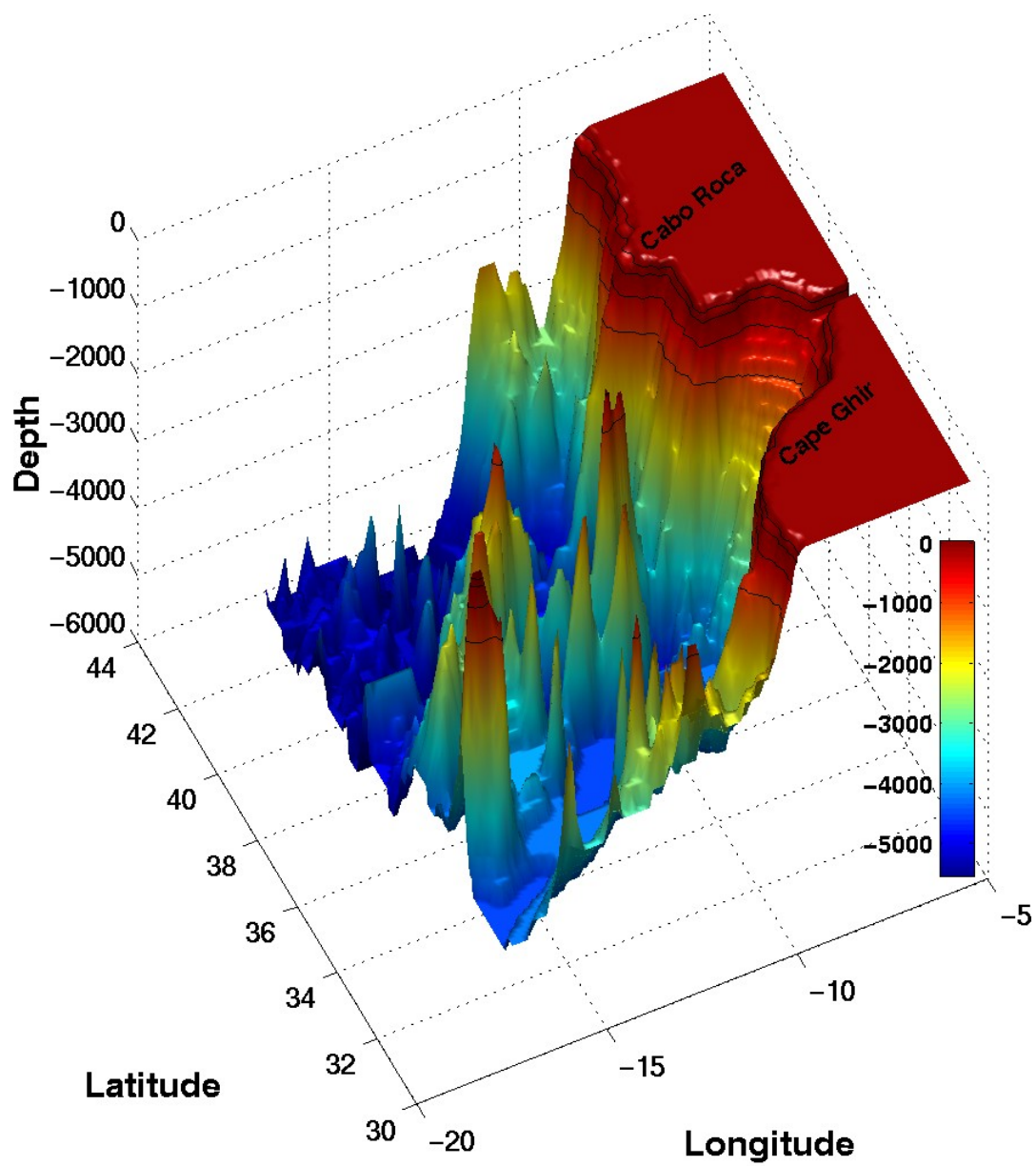
Figure 5a. Raw topography for the Northern Canary Current System, depths in meters. Contour lines at 100, 200, 500 and 1000 m depth.
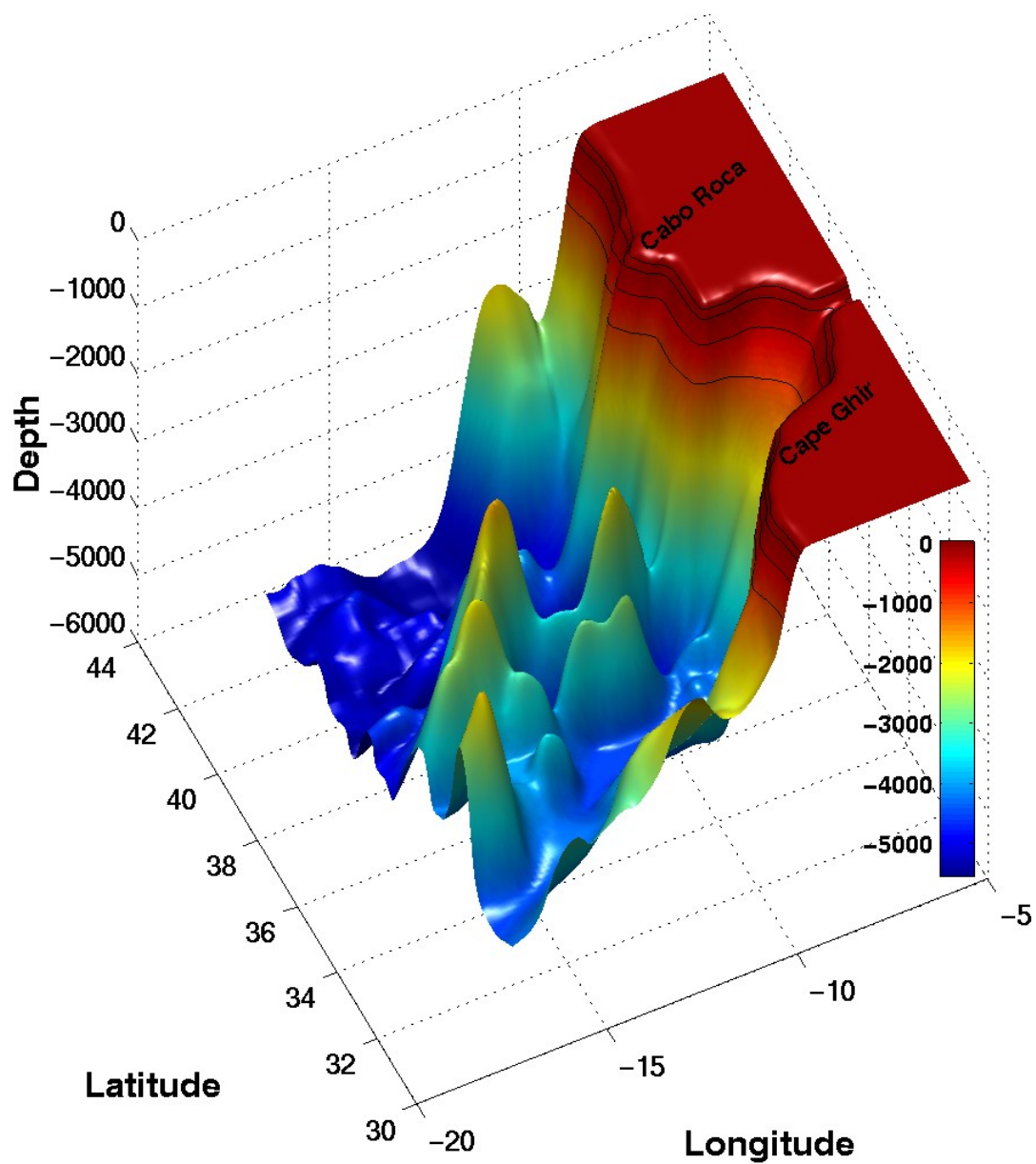
Figure 5b. Topography smoothed with a Gaussian two-dimensional filter method for the Northern Canary Current System, depths in meters. Contour lines at 100, 200, 500 and 1000 m depth.
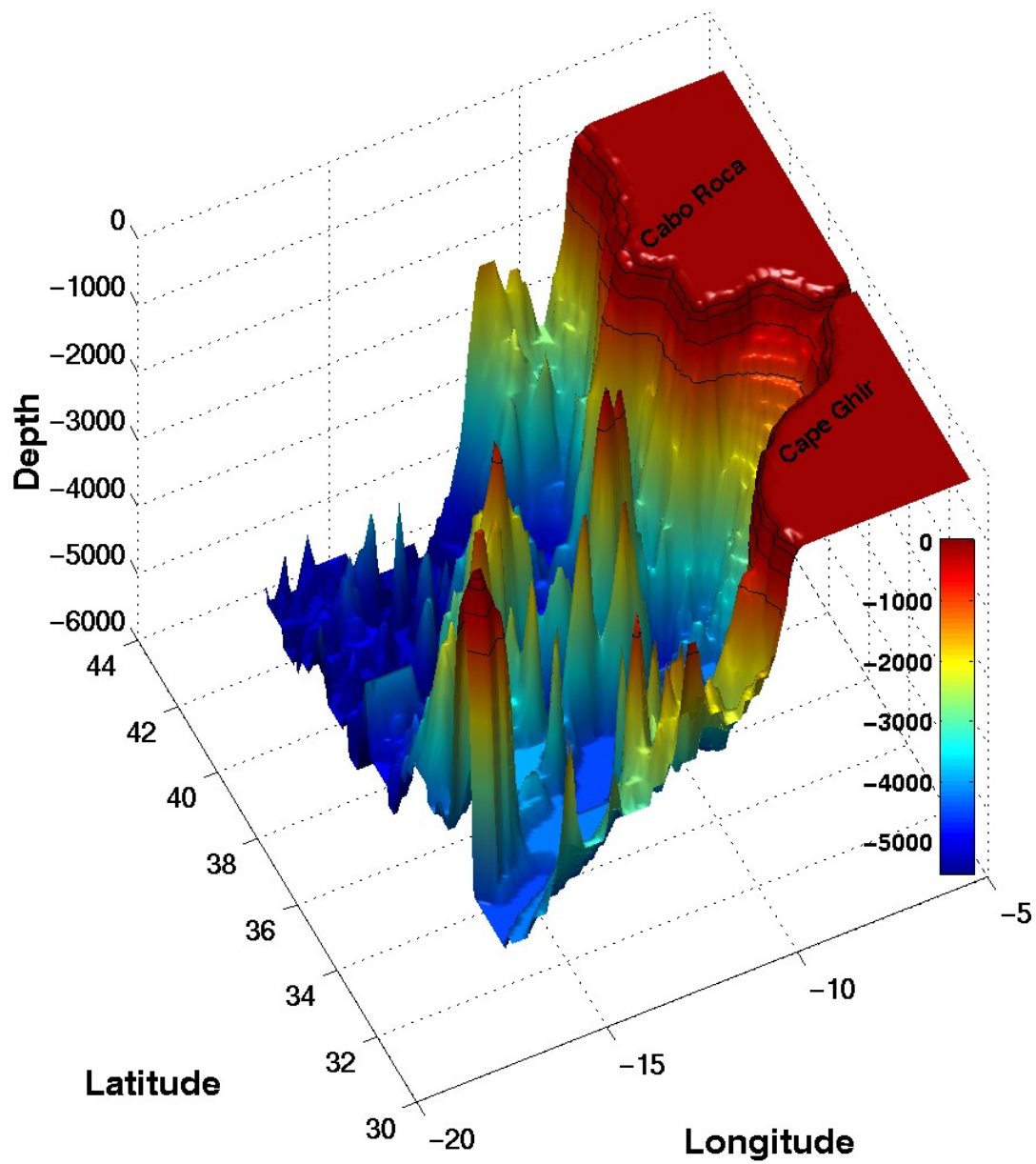
Figure 5c. Topography smoothed with the direct iterative method for the Northern Canary Current System, depths in meters. Contour lines at 100, 200, 500 and 1000 m depth.
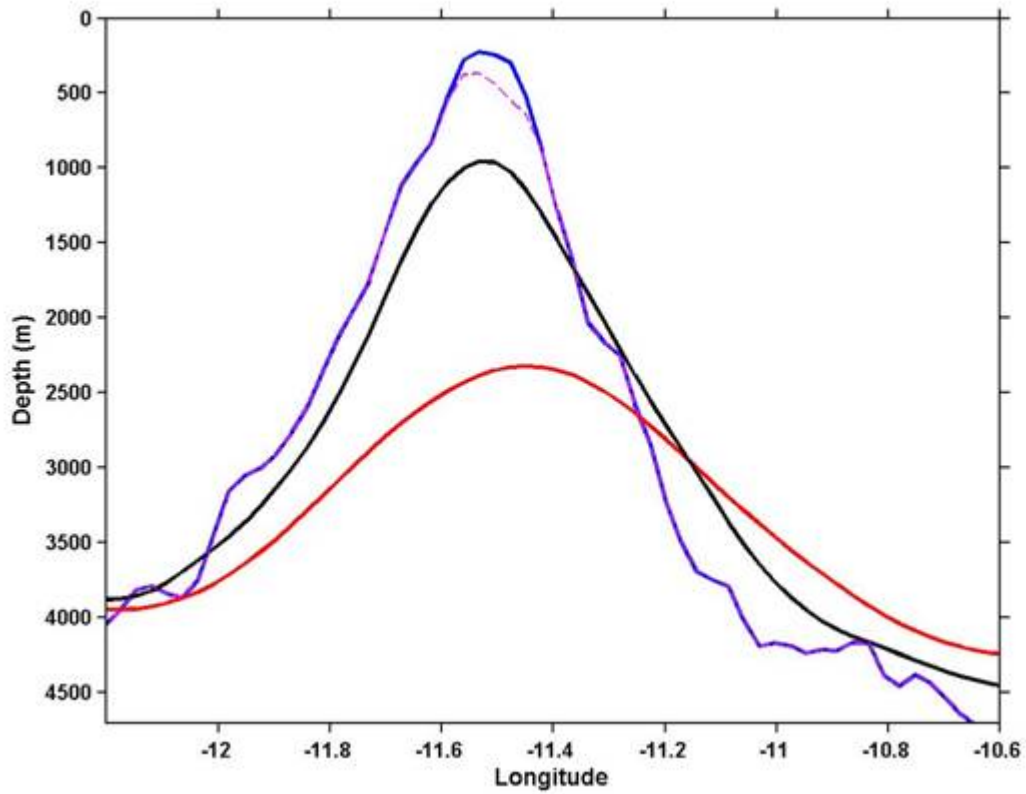
Figure 5d. Cross sections of topography across a seamount at 36.4°N showing the methods of topography smoothing. The blue line is the raw (unsmoothed topography). The red line is the topography smoothed with a Gaussian filter. The black line is the topography smoothed with the alternative POM method. The dashed magenta line is the topography smoothed using the one-dimensional direct iterative technique.

51

w/ Volume Constraint, Day 1, Surface.
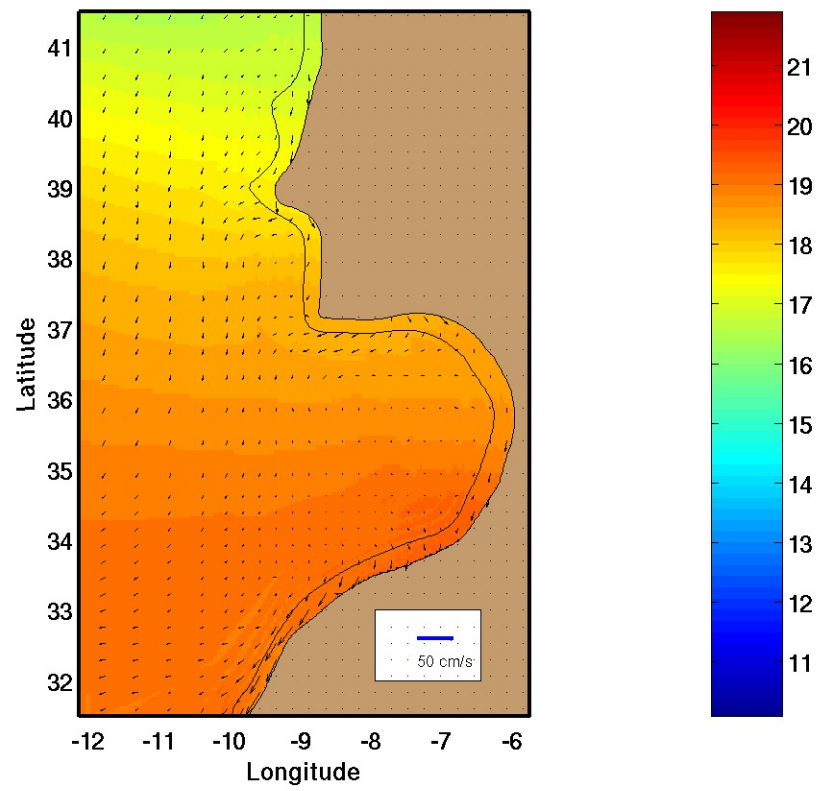
Figure 6a. Surface temperature (°C) and velocity vectors (cm/s) for day 1 with Volume Constraint.

w/ Volume Constraint, Day 90, Surface.
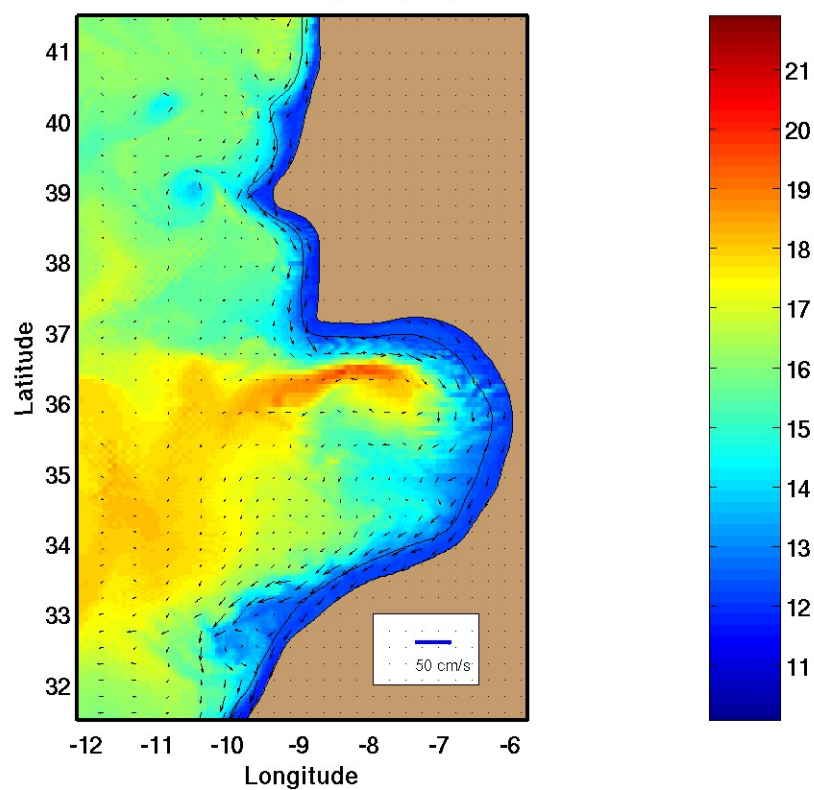
Figure 6b. Surface temperature (°C) and velocity vectors (cm/s) for day 90 with Volume Constraint.

w/o Volume Constraint, Day 1, Surface.
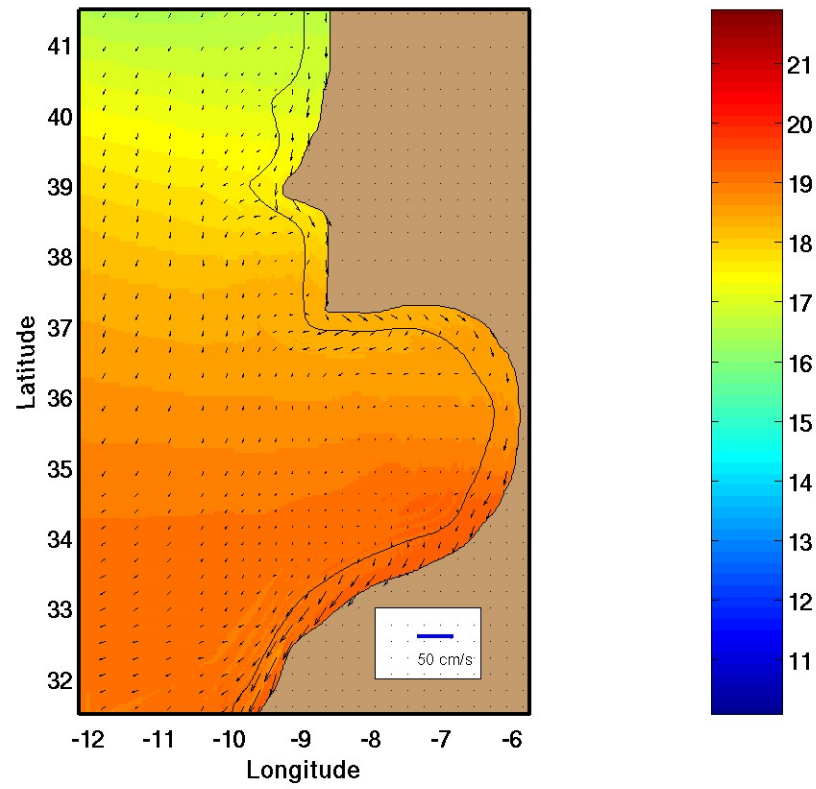
Figure 7a. Surface temperature (°C) and velocity vectors (cm/s) for day 1 without Volume Constraint.

w/o Volume Constraint, Day 90, Surface.
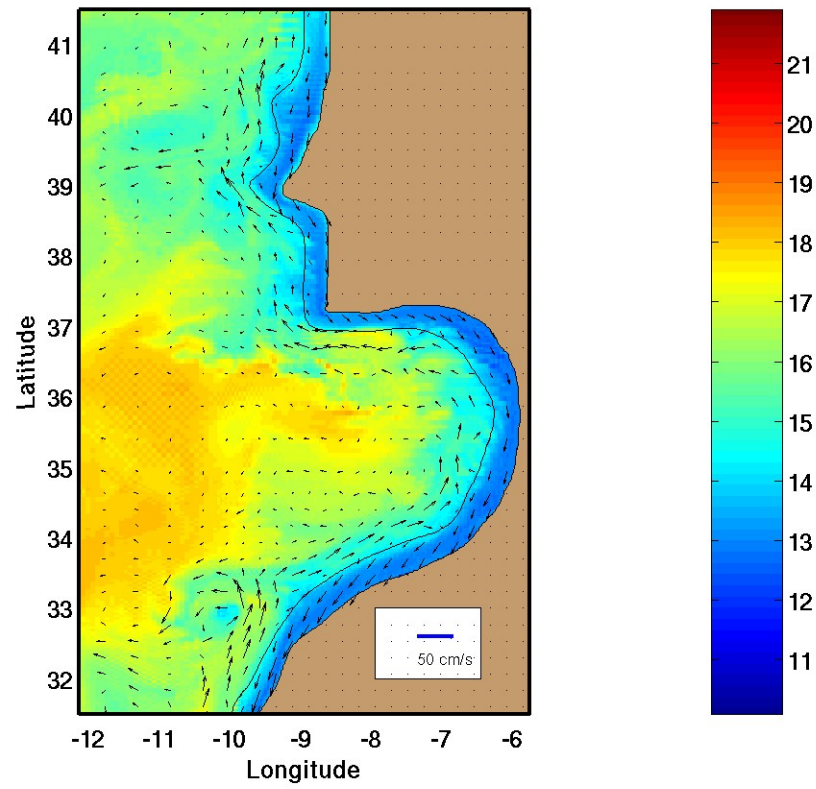
Figure 7b. Surface temperature (°C) and velocity vectors (cm/s) for day 90 without Volume Constraint.
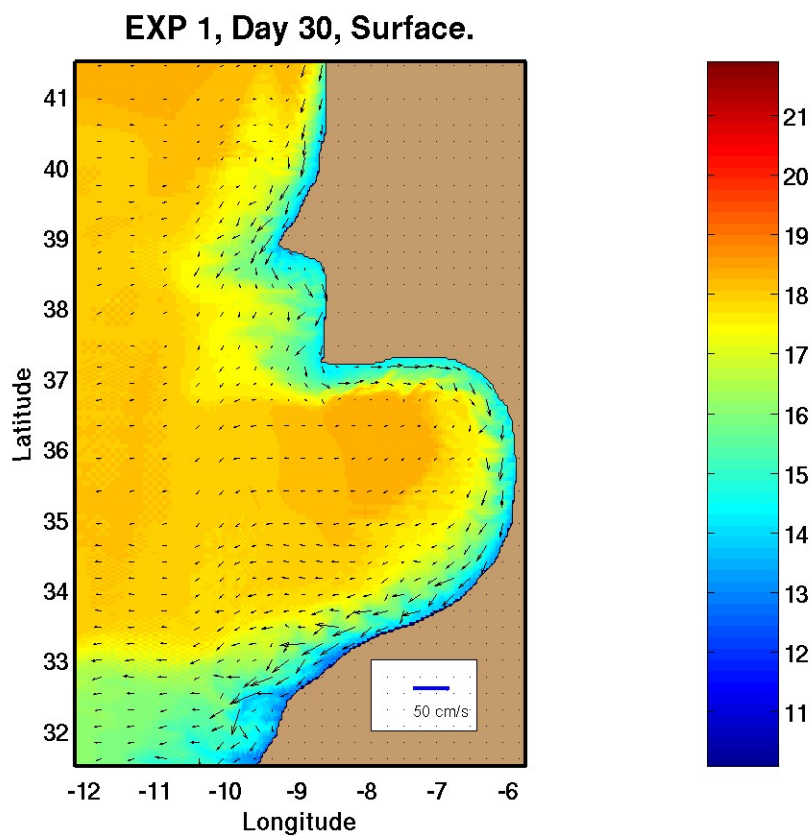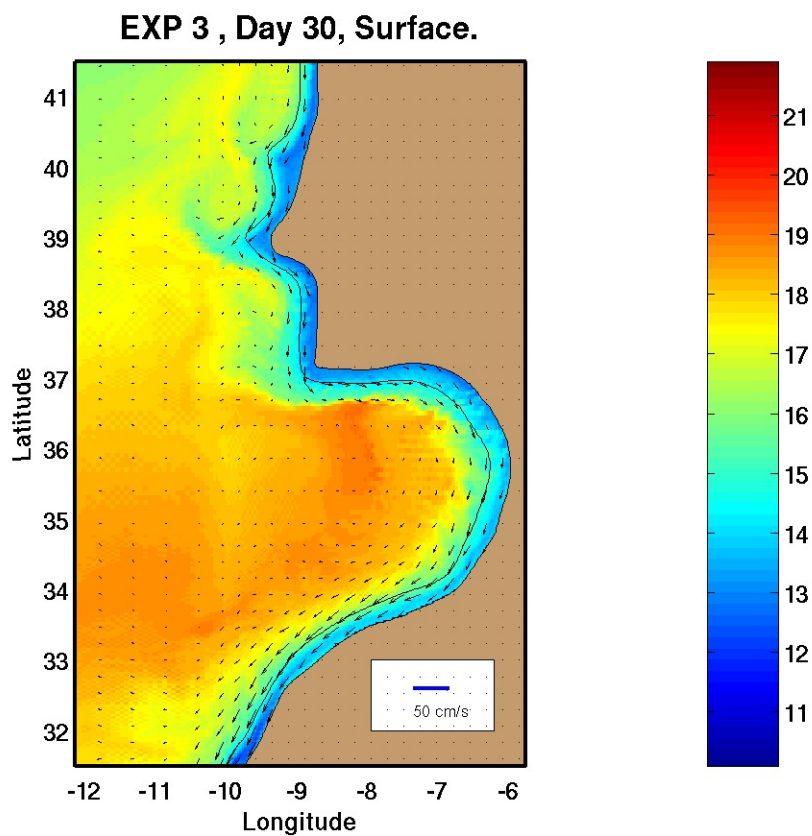
Figure 8a. Surface temperature (°C) and velocity vectors (cm/s) on day 30 for Experiment 1.
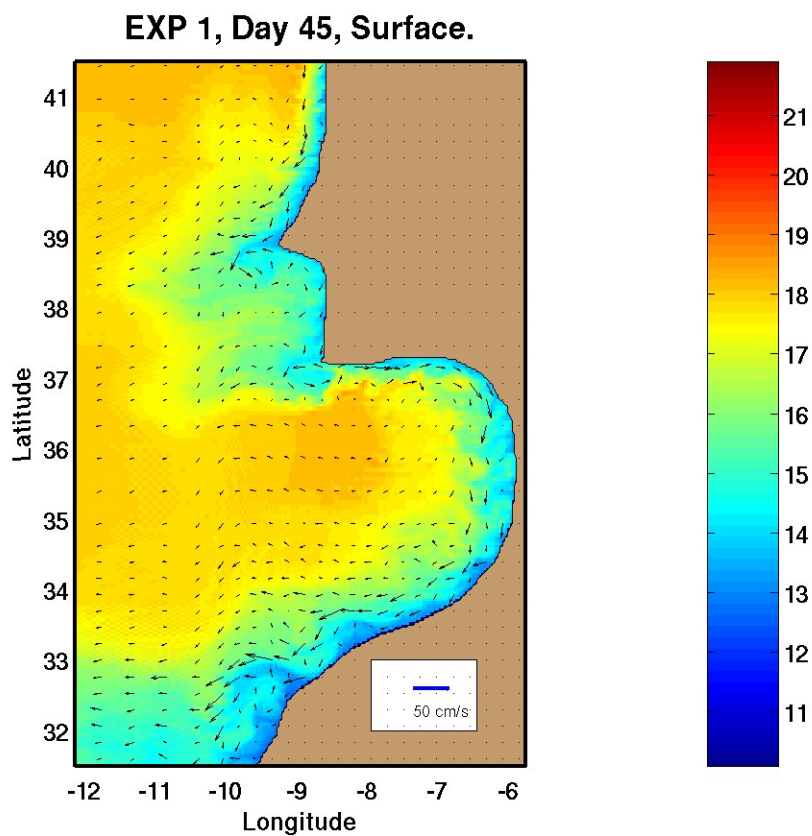
Figure 8b. Surface temperature (°C) and velocity vectors (cm/s) on day 45 for Experiment 1.

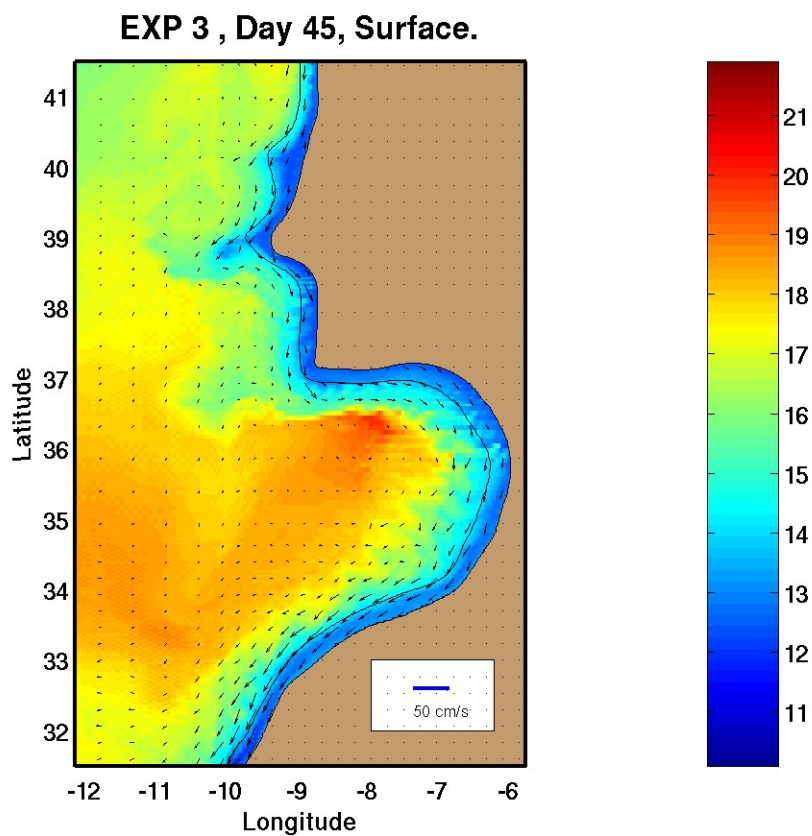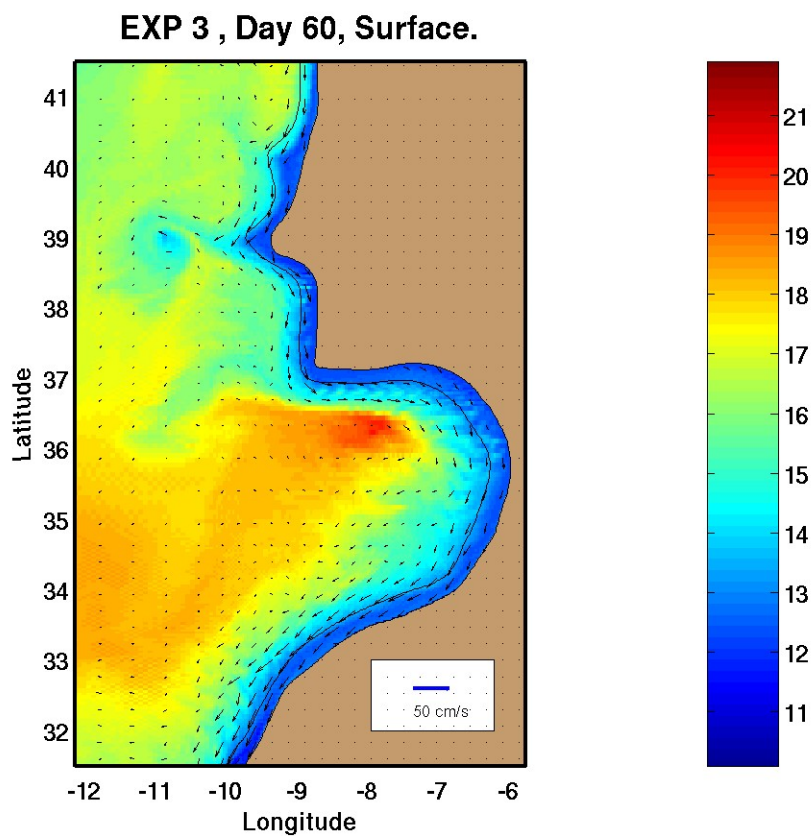**EXP 1, Day 60, Surface.**
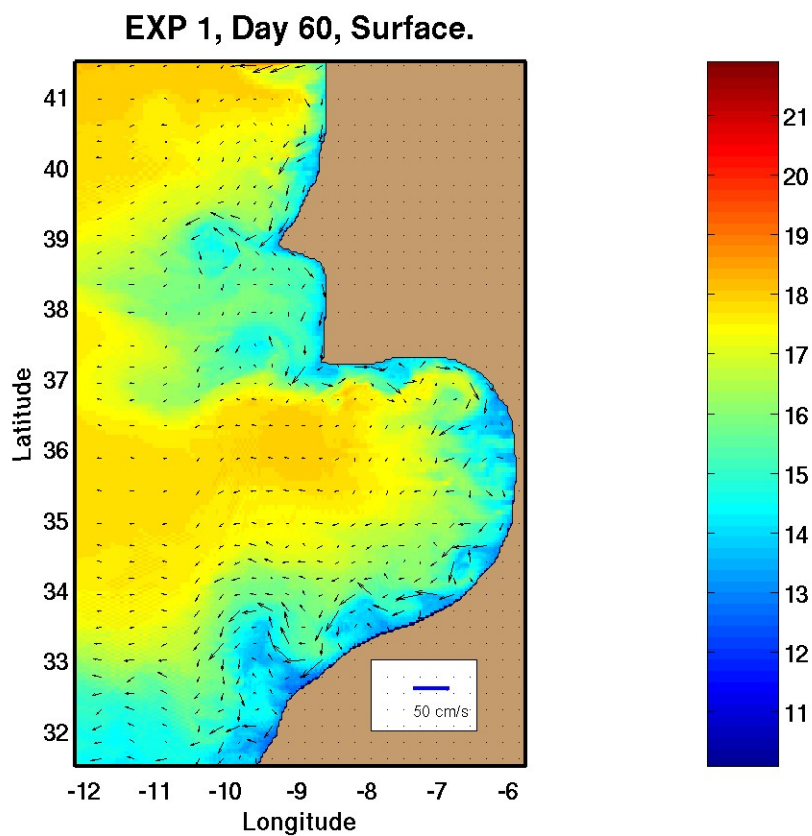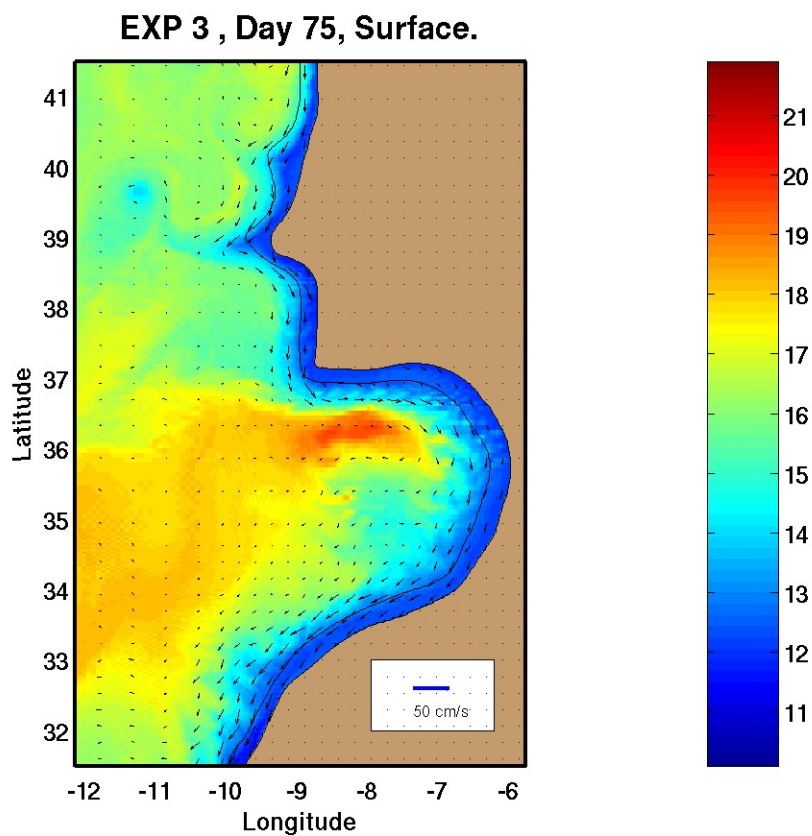
Figure 8c. Surface temperature (°C) and velocity vectors (cm/s) on day 60 for Experiment 1.

EXP 1, Day 75, Surface.
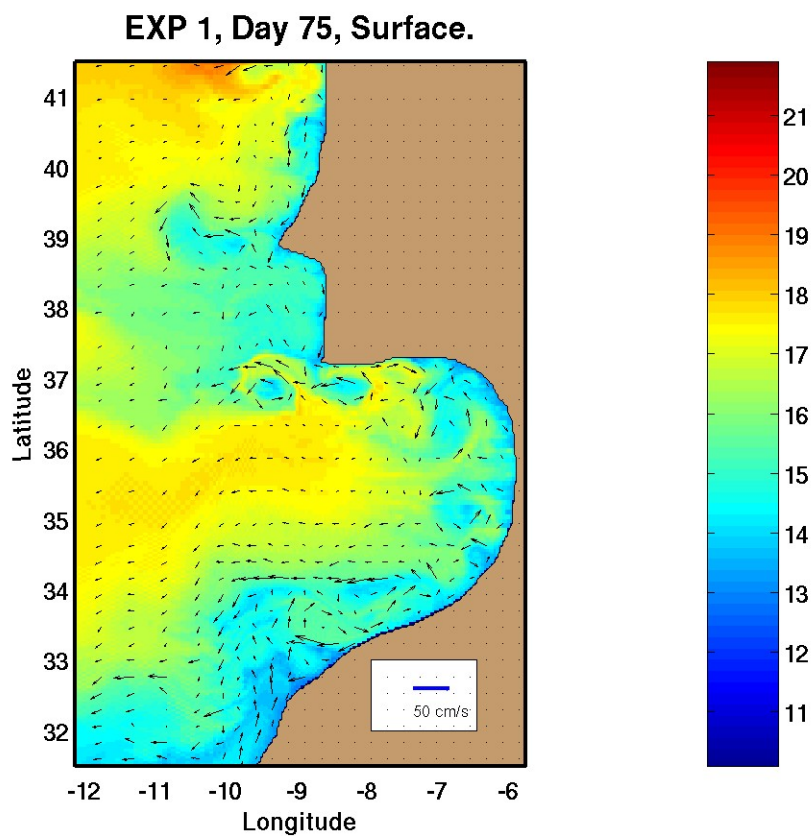
Figure 8d. Surface temperature (°C) and velocity vectors (cm/s) on day 60 for Experiment 1.
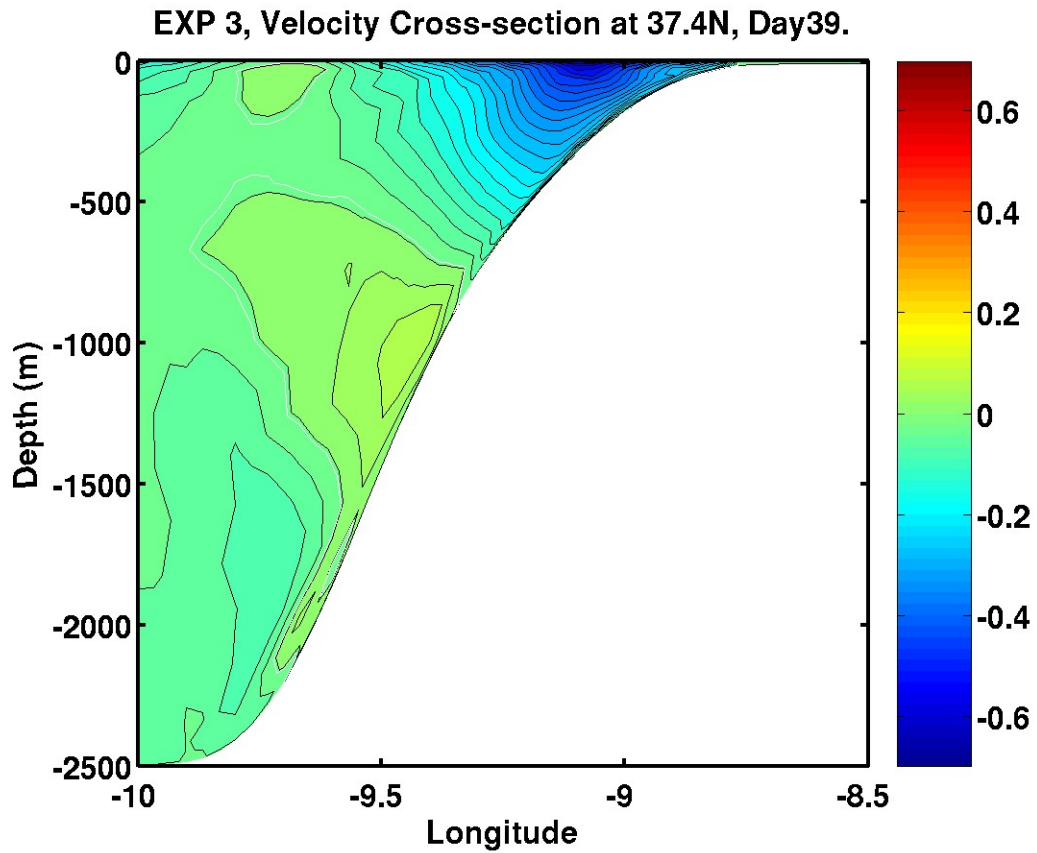
EXP 1, Velocity Cross-section at 37.4N, Day39.
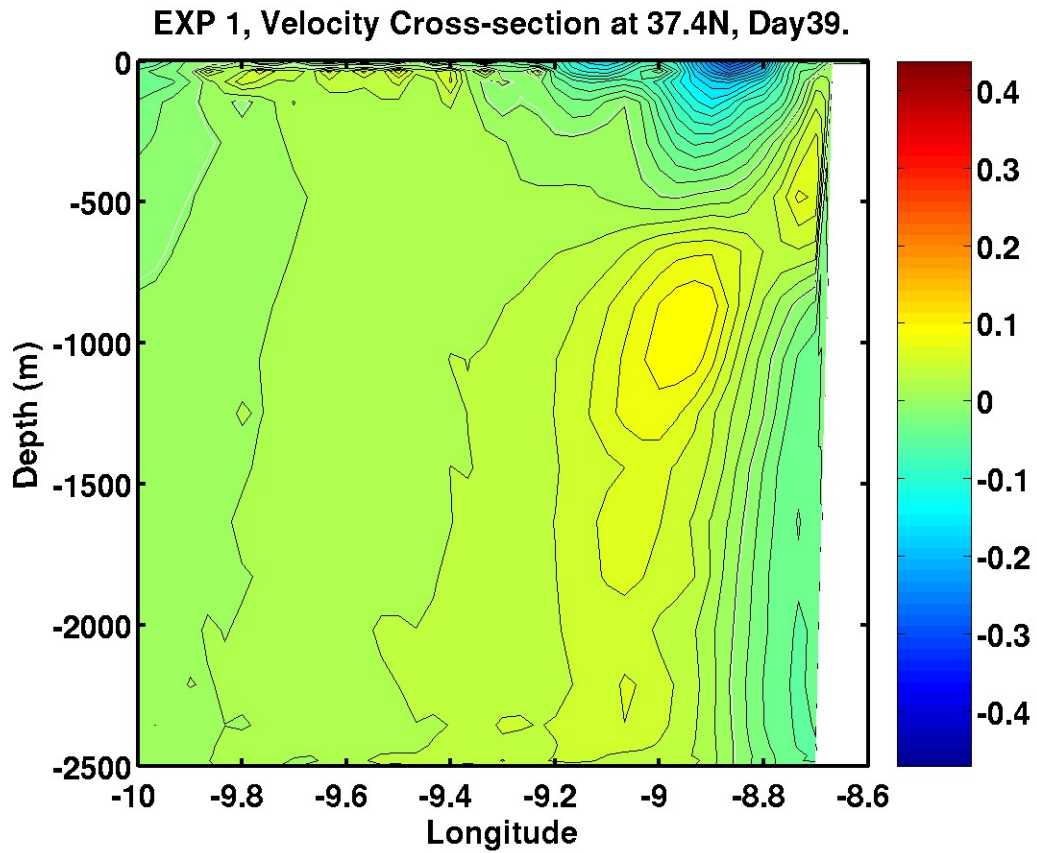
Figure 8e. Velocity (m/s) cross-section at 37.4°N on day 39
for Experiment 1.
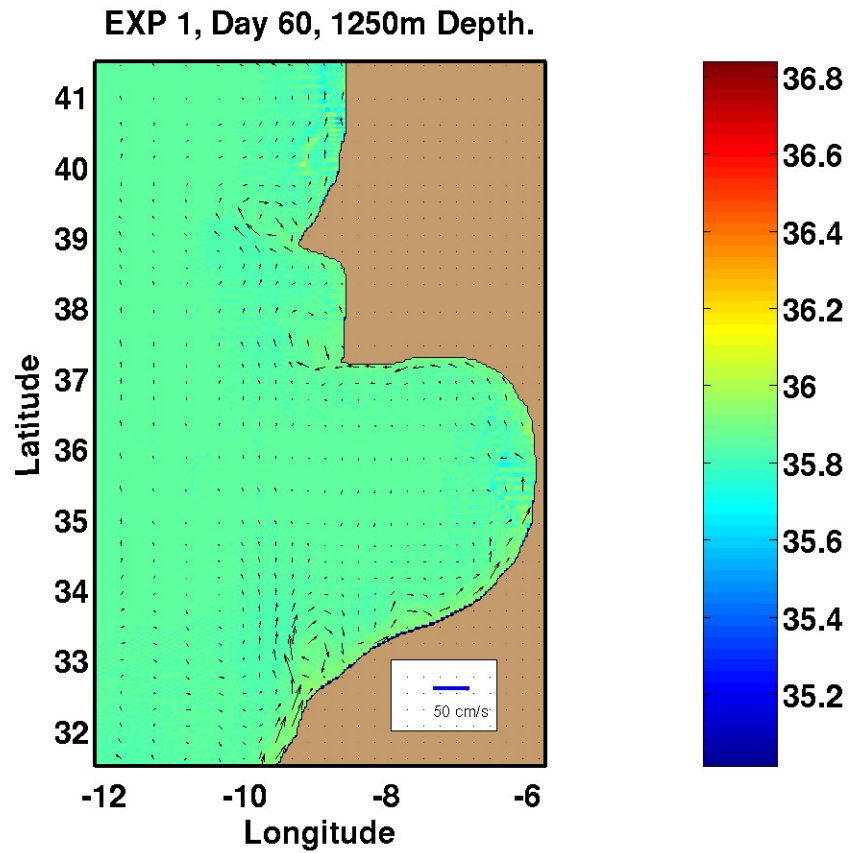
Figure 8f. Salinity (psu) and velocity vectors (cm/s) at
1250 m depth on day 60 for Experiment 1.
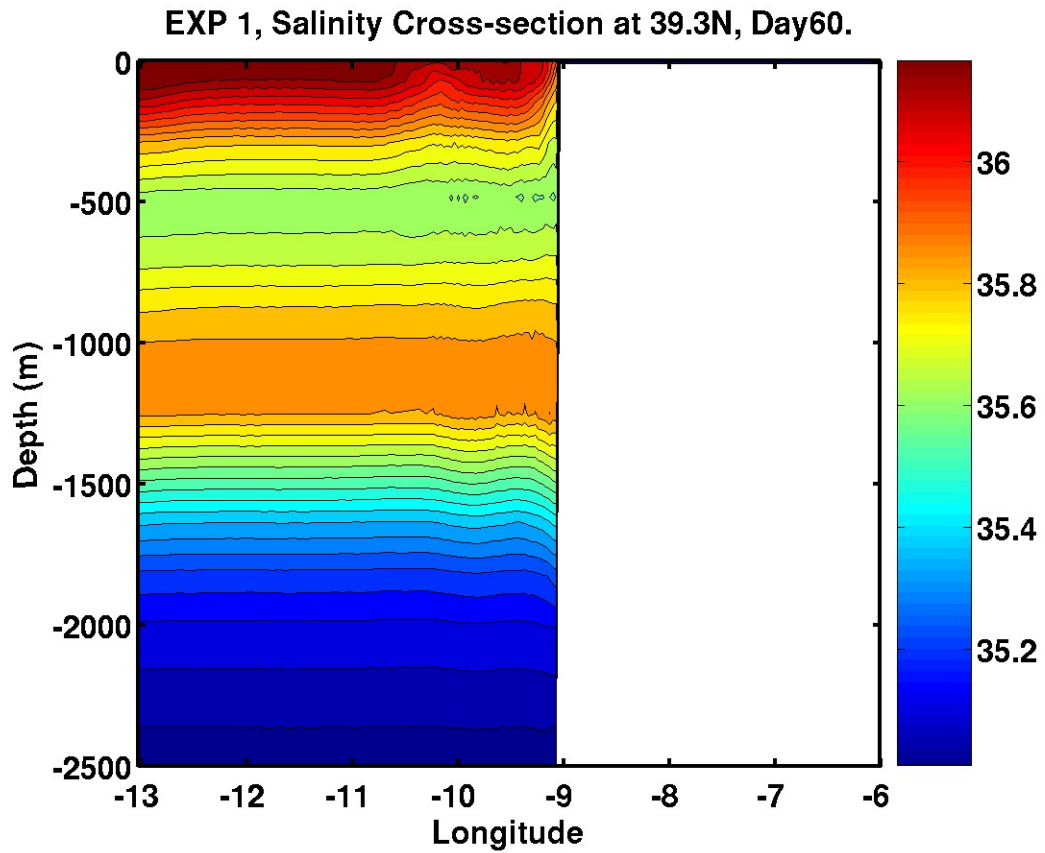
Figure 8g. Salinity (psu) cross-section at 39.3°N on day 60 for Experiment 1.

EXP 2, Day 30, Surface.
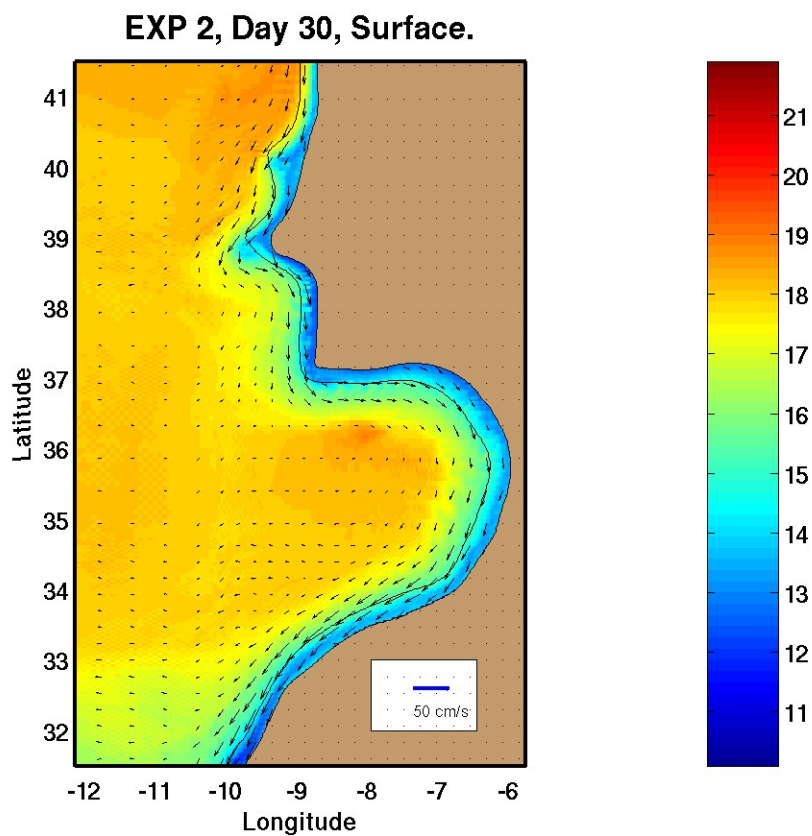
Figure 9a. Surface temperature (°C) and velocity vectors (cm/s) on day 30 for Experiment 2.

EXP 2, Day 45, Surface.
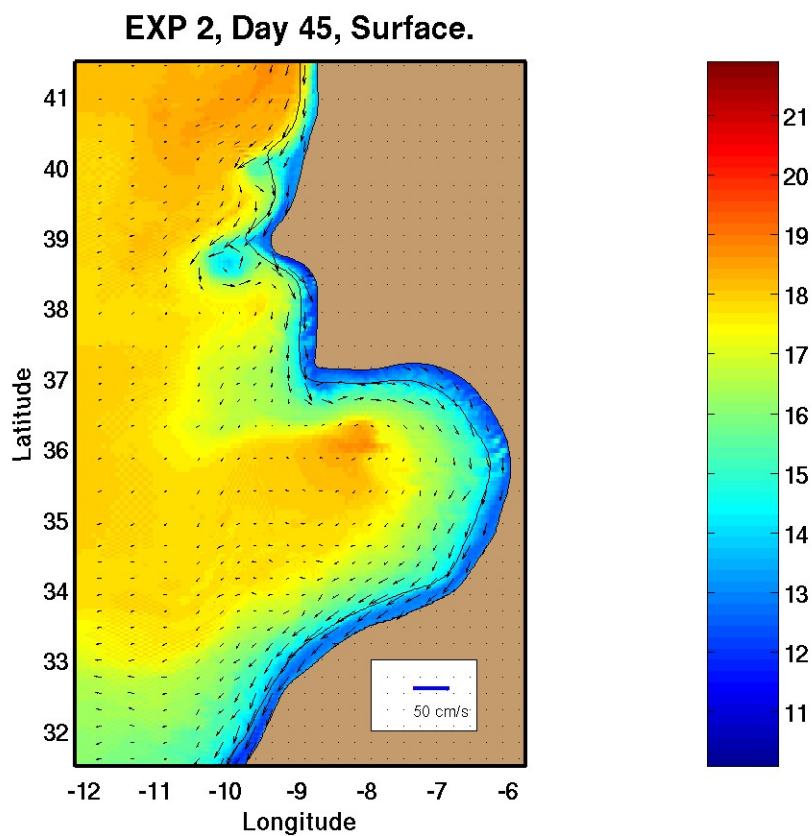
Figure 9b. Surface temperature (°C) and velocity vectors (cm/s) on day 45 for Experiment 2.

EXP 2, Day 60, Surface.
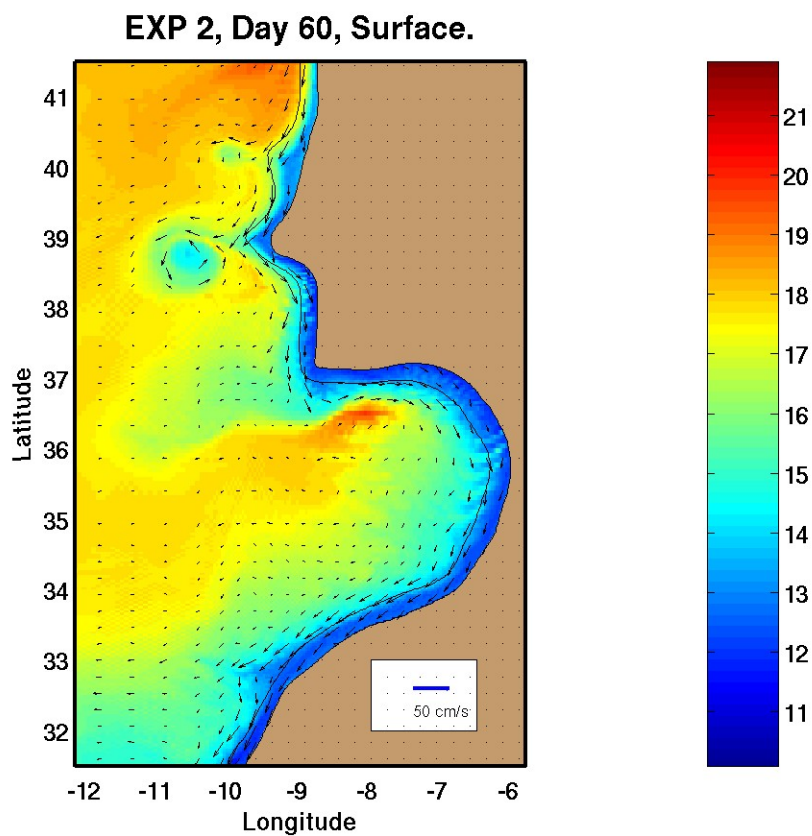
Figure 9c. Surface temperature (°C) and velocity vectors (cm/s) on day 60 for Experiment 2.

EXP 2, Day 75, Surface.
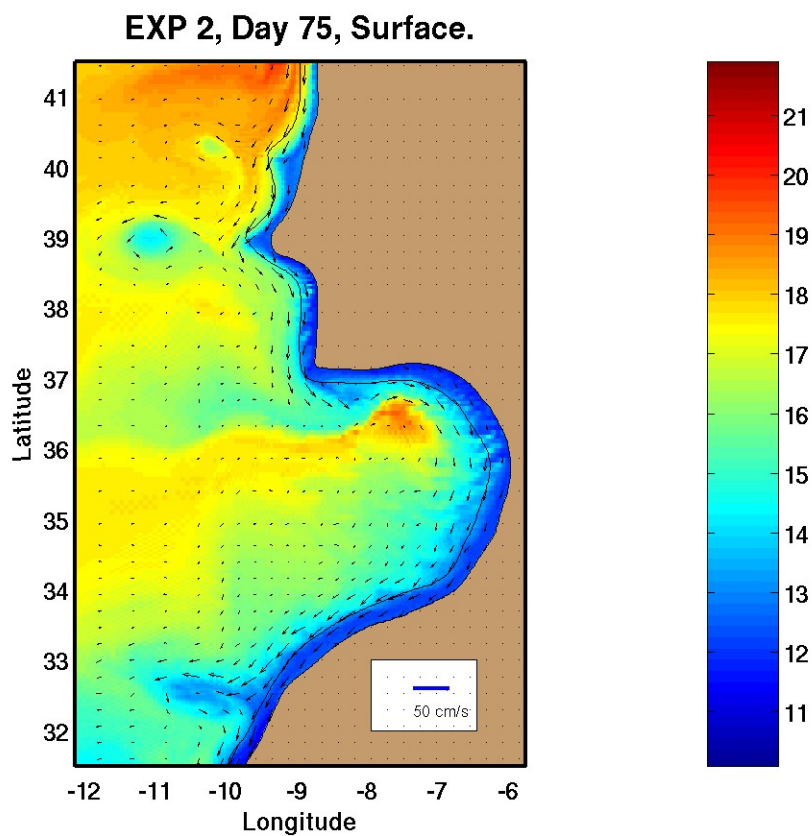
Figure 9d. Surface temperature (°C) and velocity vectors (cm/s) on day 75 for Experiment 2.
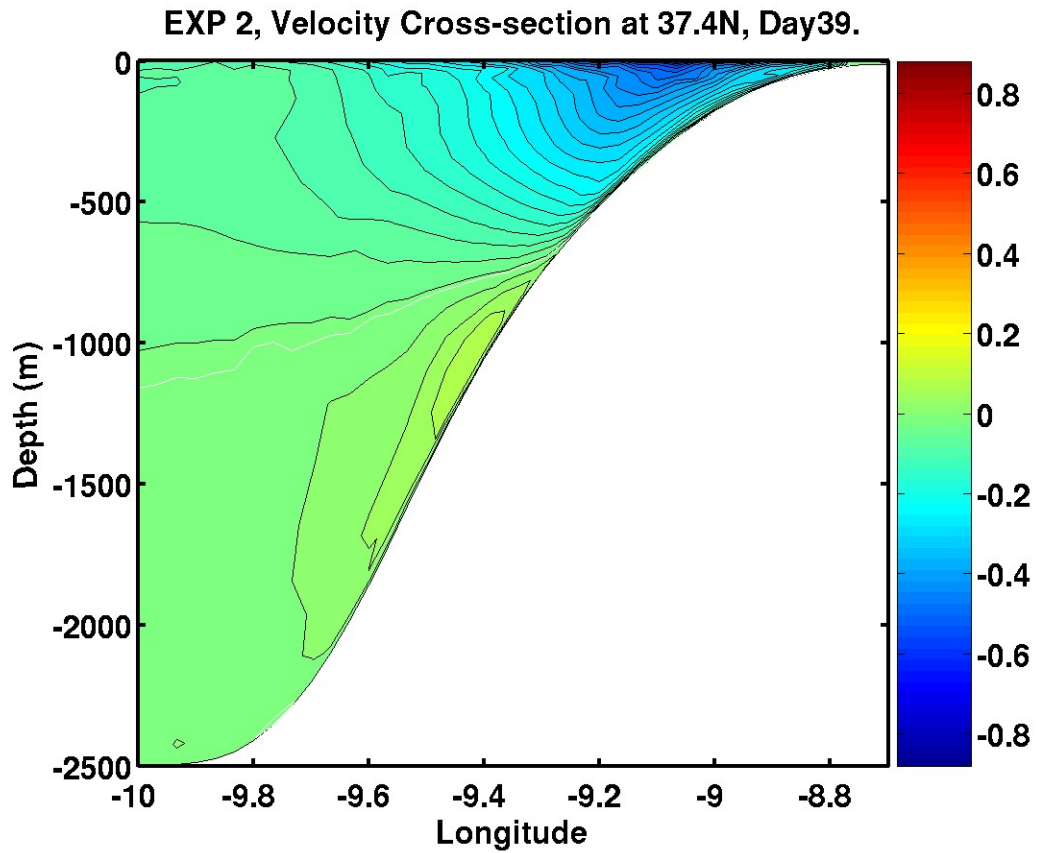
Figure 9e. Velocity (m/s) cross-section at 37.4°N on day 39
for Experiment 2.
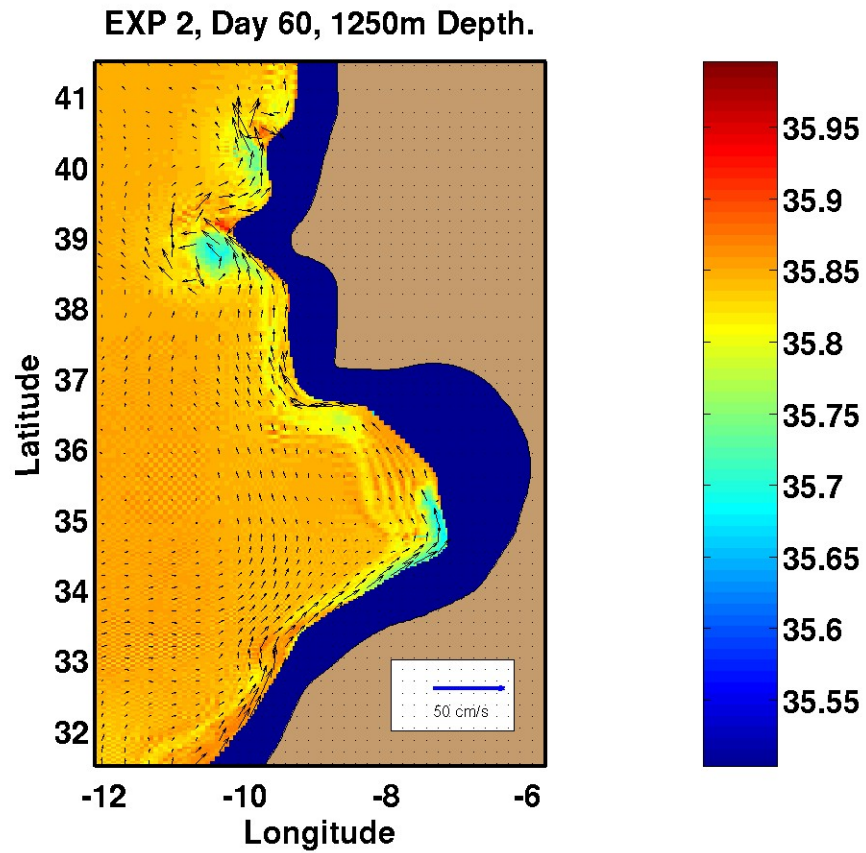
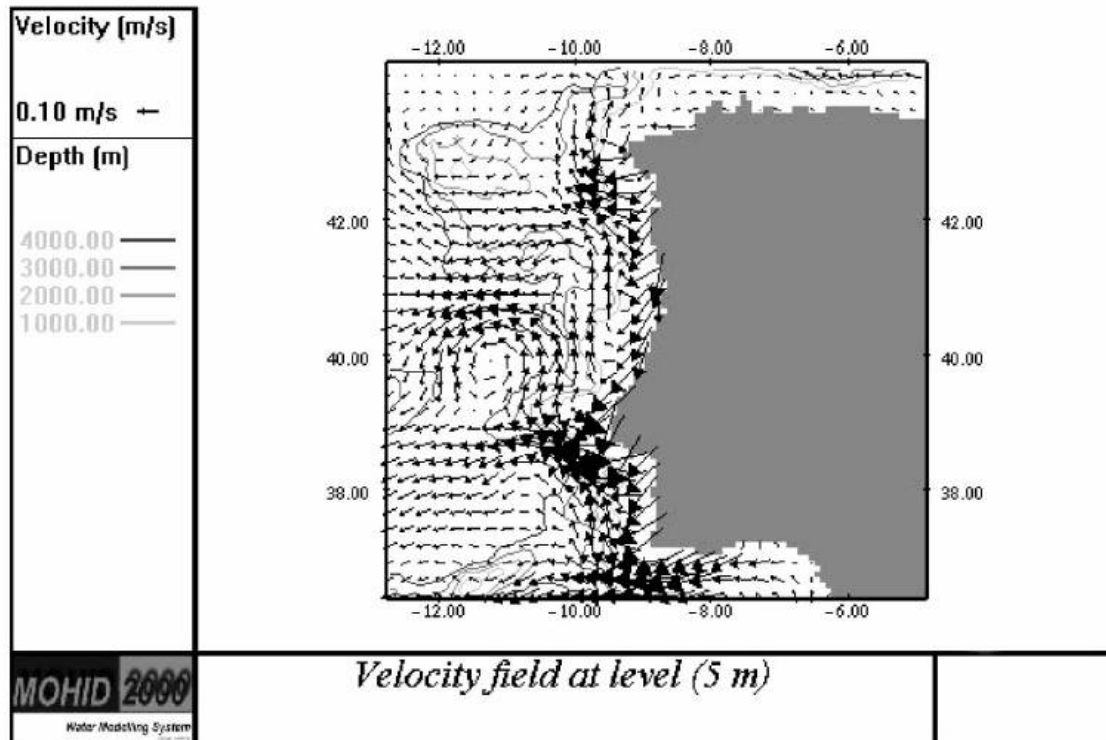Figure 9f. Salinity (psu) and velocity vectors (cm/s) at 1250 m depth on day 60 for Experiment 2.

EXP 3 , Day 5, Surface.
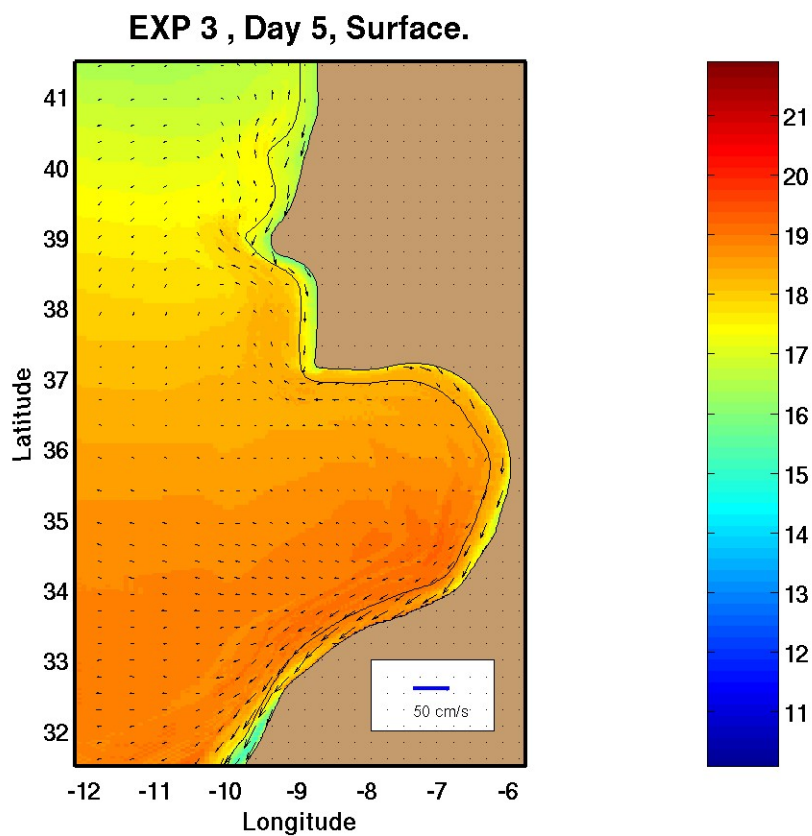
Figure 10a. Surface temperature (°C) and velocity vectors (cm/s) on day 5 for Experiment 3.

EXP 3 , Day 30, Surface.

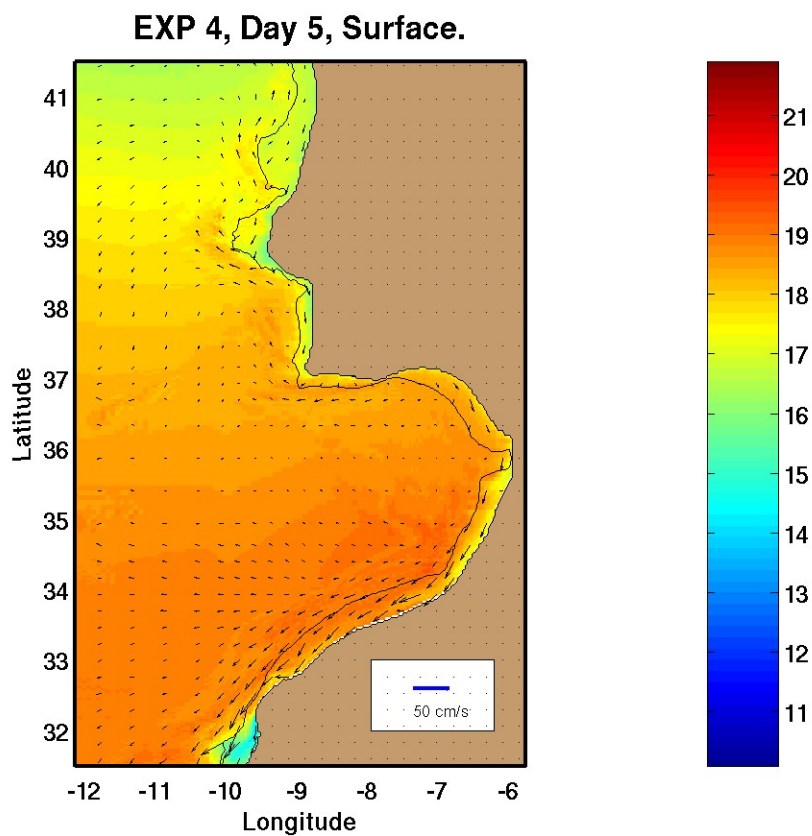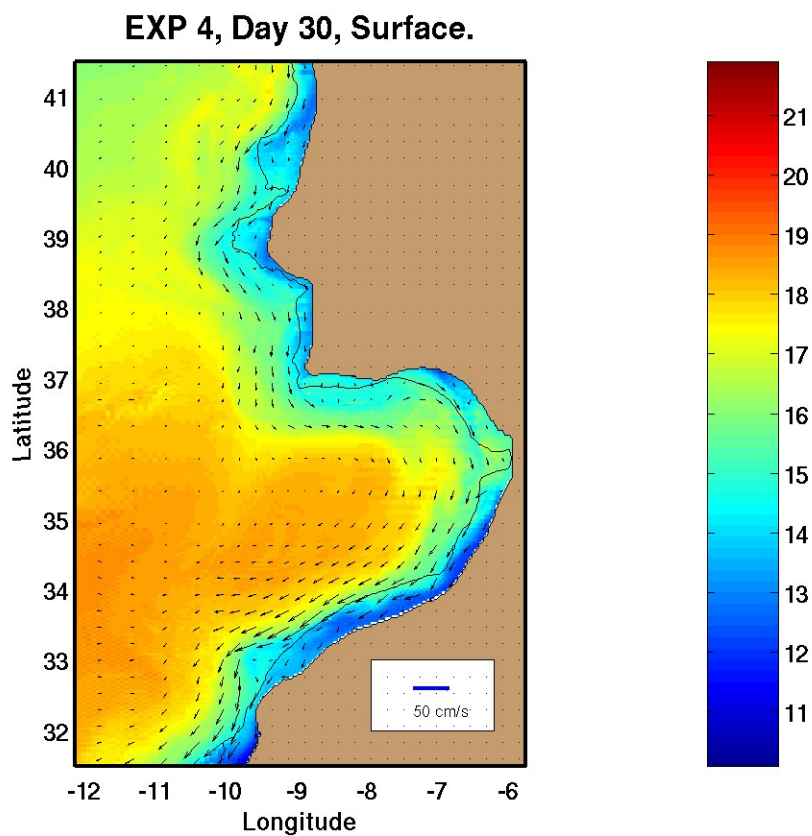Figure 10b. Surface temperature (°C) and velocity vectors (cm/s) on day 30 for Experiment 3.

EXP 3 , Day 45, Surface.

Figure 10c. Surface temperature (°C) and velocity vectors (cm/s) on day 45 for Experiment 3.

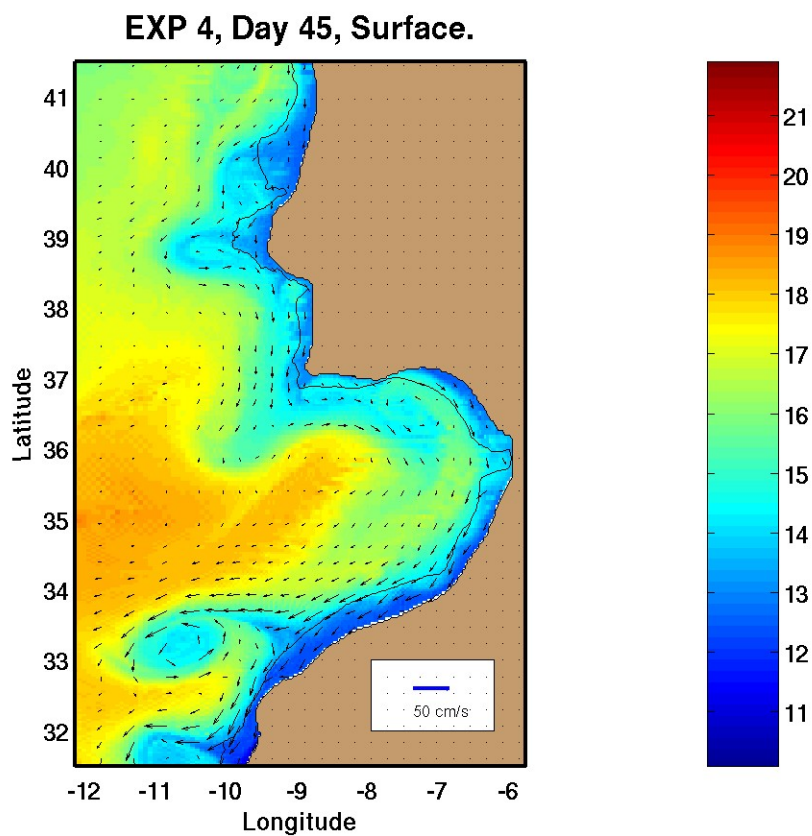Figure 10d. Surface temperature (°C) and velocity vectors (cm/s) on day 60 for Experiment 3.

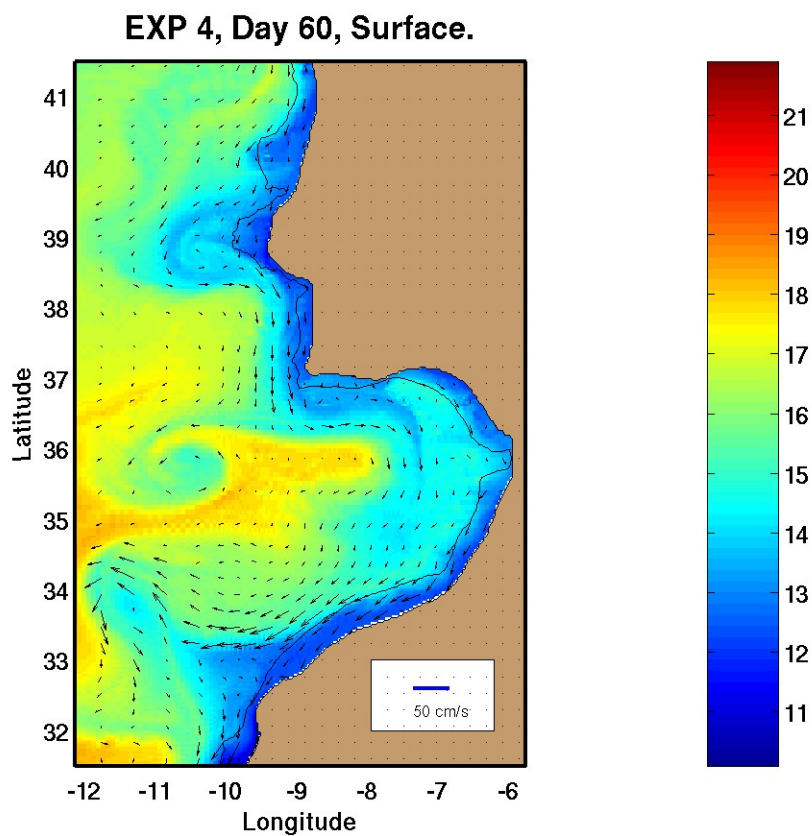**EXP 3 , Day 75, Surface.**
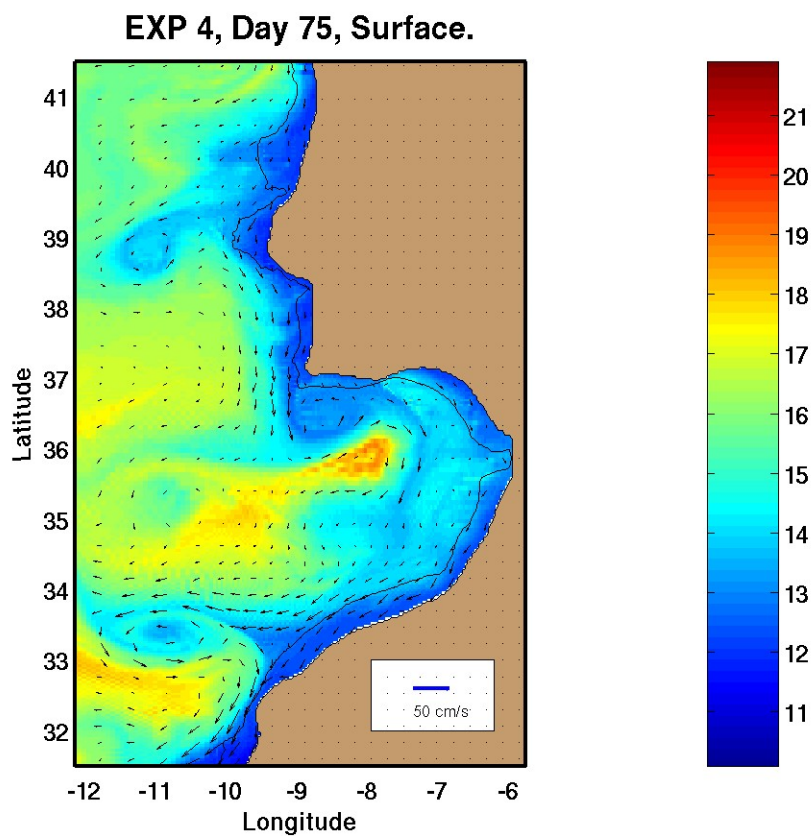
Figure 10e. Surface temperature (°C) and velocity vectors (cm/s) on day 75 for Experiment 3.

Figure 10f. Velocity (m/s) cross-section at 37.4°N on day 39 for Experiment 3.
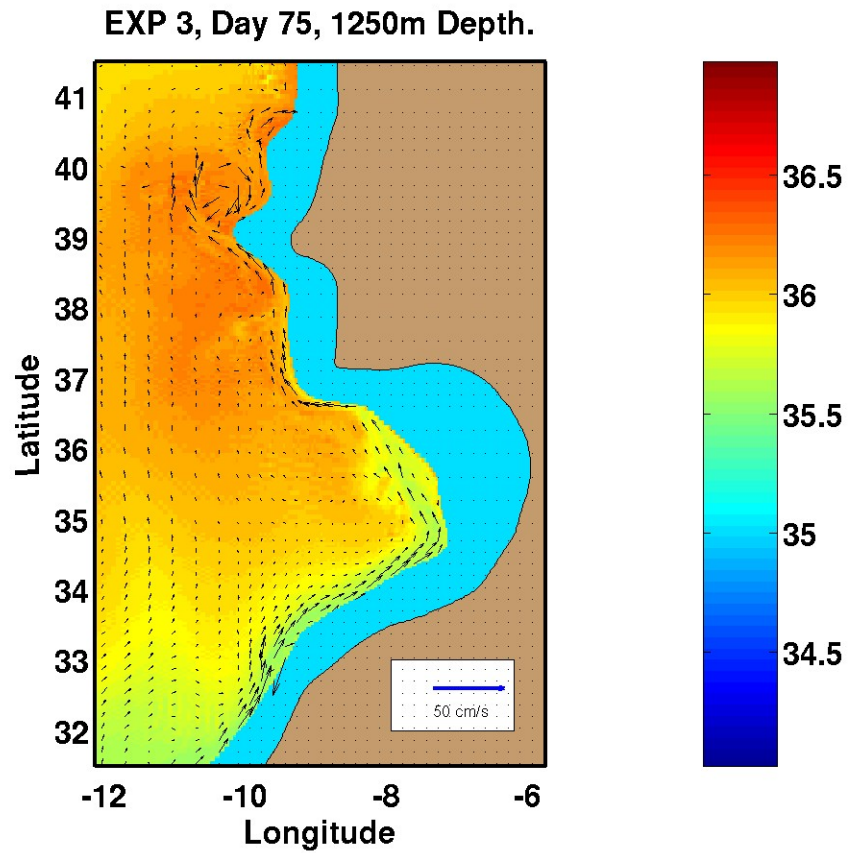
Figure 10g. Salinity (psu) and velocity vectors (cm/s) at 1250 m depth on day 75 for Experiment 3.

Figure 11. Zoom of monthly averaged velocity field at level
1 (5 m) for July 1994. To avoid clutter, the velocity
vectors are plotted every second grid point in both
directions (from Coelho et al. (2002) Figure 15).

EXP 4, Day 5, Surface.

Figure 12a. Surface temperature (°C) and velocity vectors (cm/s) on day 5 for Experiment 4.

EXP 4, Day 30, Surface.

Figure 12b. Surface temperature (°C) and velocity vectors (cm/s) on day 30 for Experiment 4.

Figure 12c. Surface temperature (°C) and velocity vectors (cm/s) on day 45 for Experiment 4.

EXP 4, Day 60, Surface.
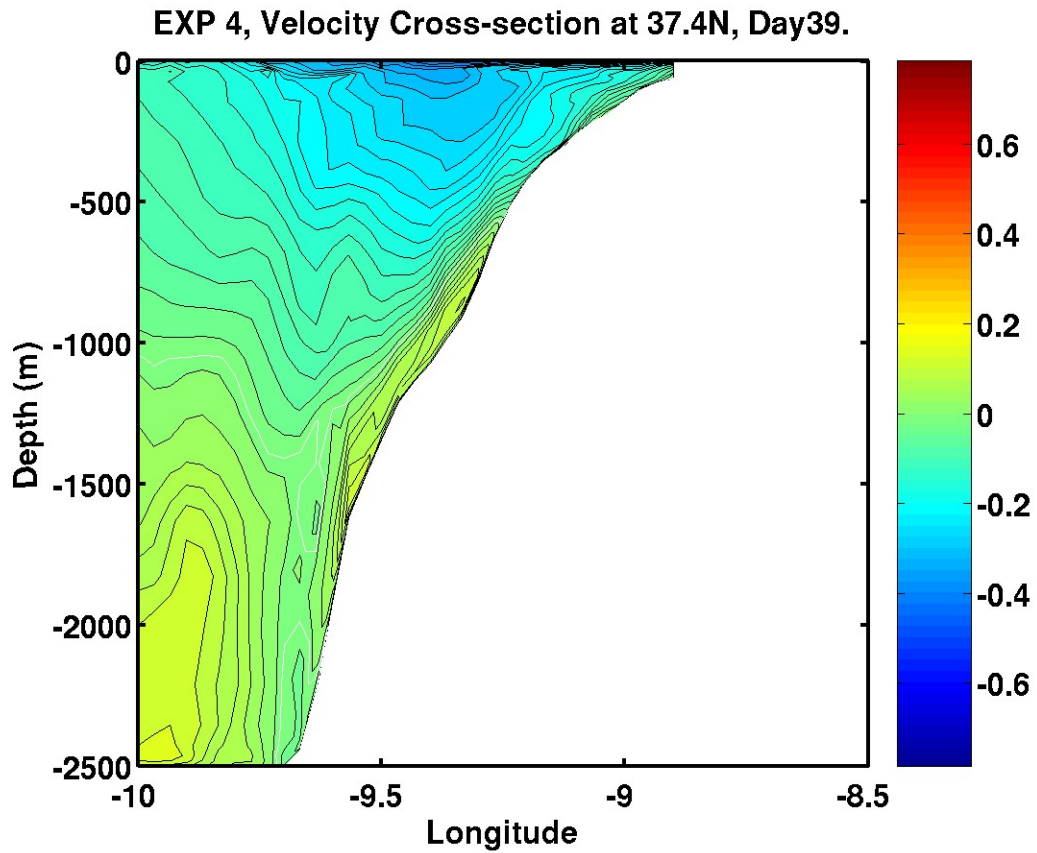

Figure 12d. Surface temperature (°C) and velocity vectors (cm/s) on day 60 for Experiment 4.

EXP 4, Day 75, Surface.

Figure 12e. Surface temperature (°C) and velocity vectors (cm/s) on day 75 for Experiment 4.

Figure 12f. Velocity (m/s) cross-section at 37.4°N on day
39 for Experiment 4.
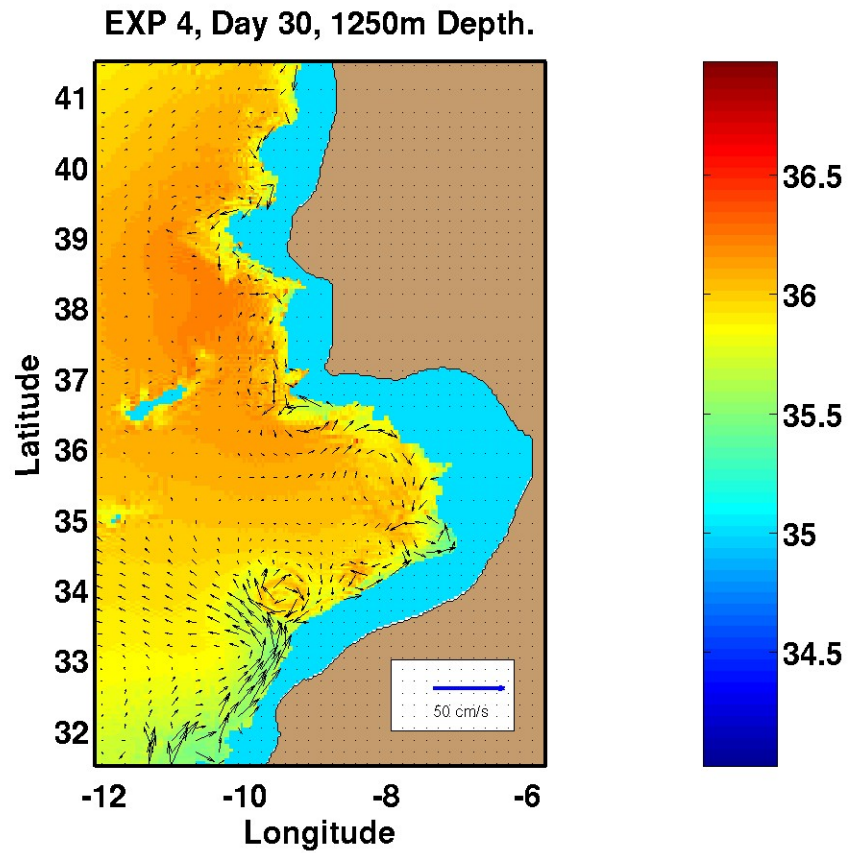
EXP 4, Day 30, 1250m Depth.

Figure 12g. Salinity (psu) and velocity vectors (cm/s) at 1250 m depth on day 30 for Experiment 4.
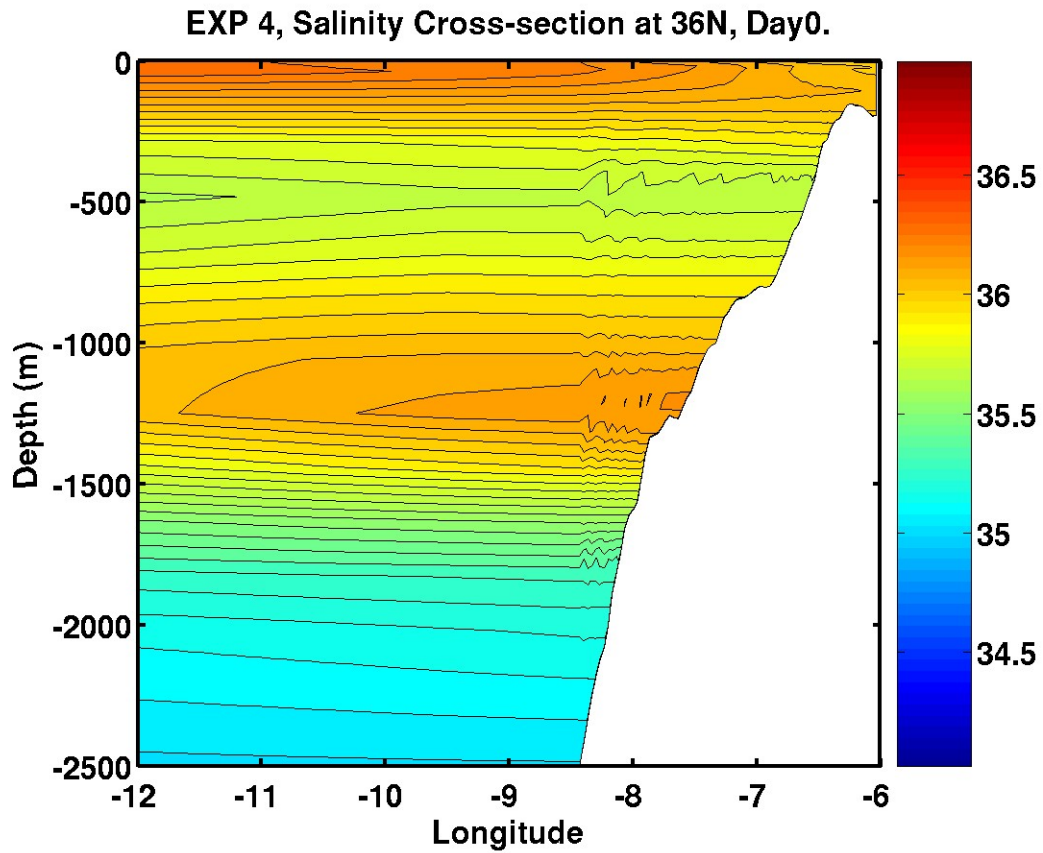
Figure 13a. Salinity (psu) cross-section at 36°N on day 0 for Experiment 4.
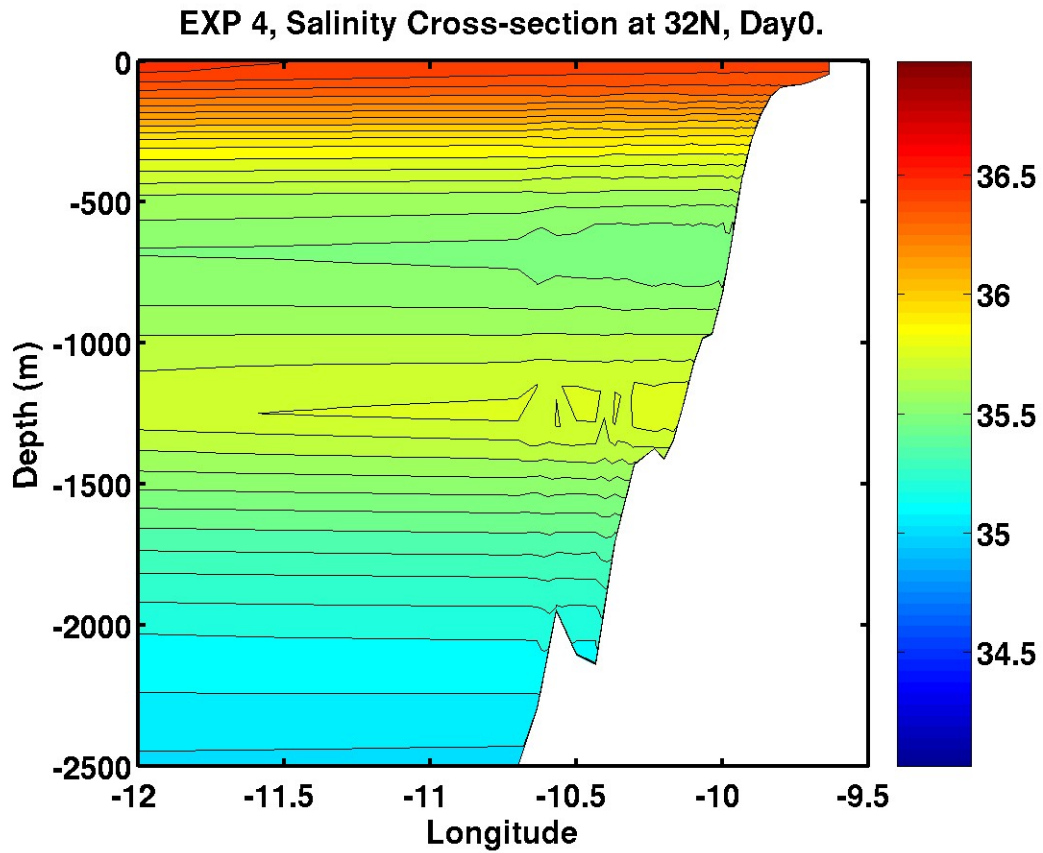
Figure 13b. Salinity (psu) cross-section at 32°N on day 0 for Experiment 4.
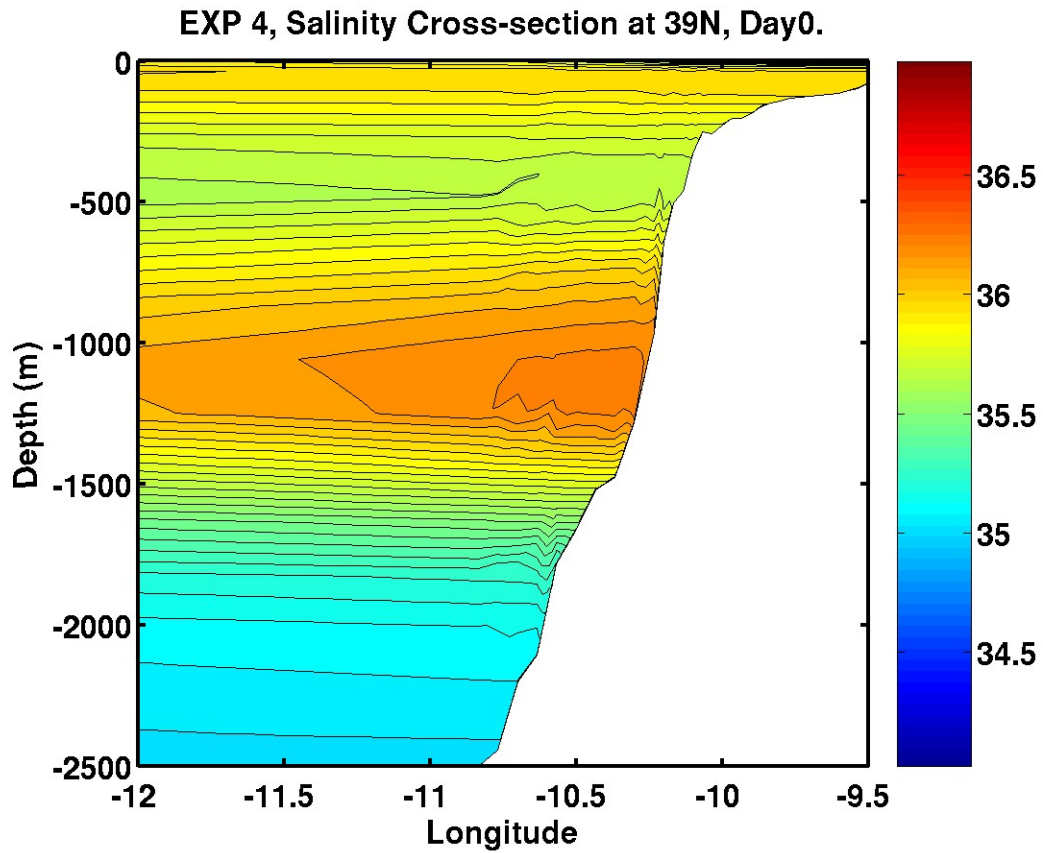
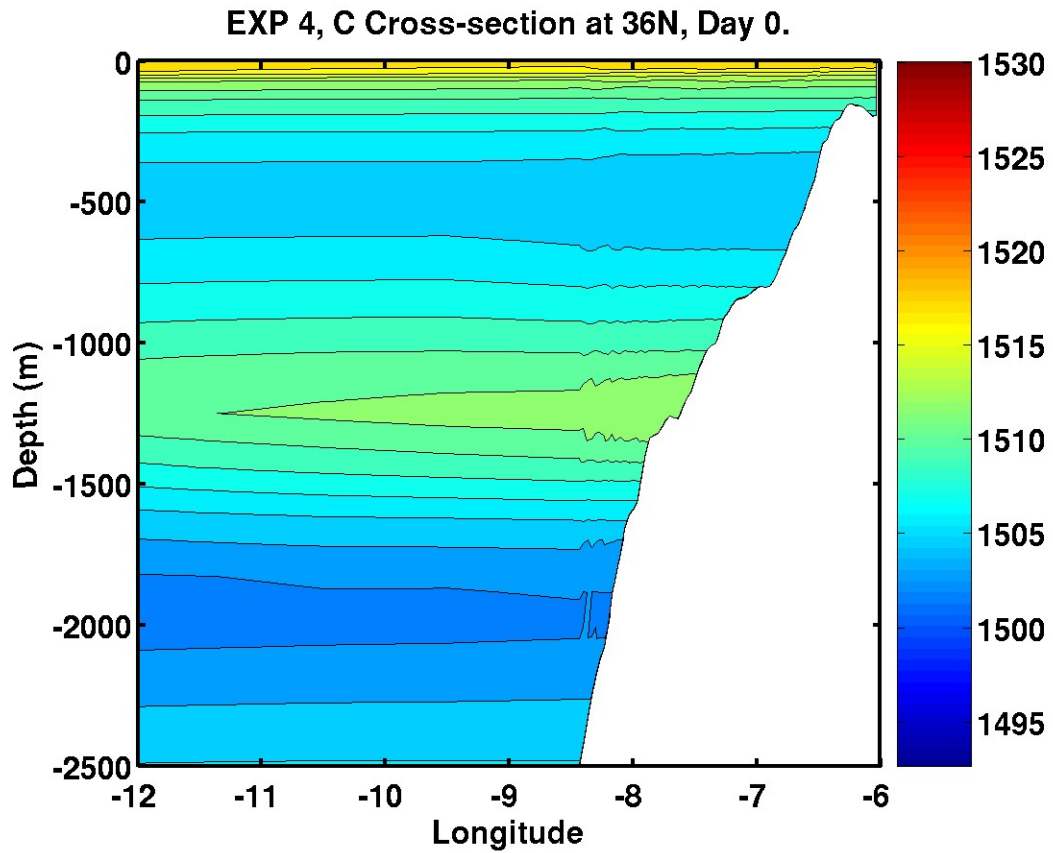Figure 13c. Salinity (psu) cross-section at 39°N on day 0 for Experiment 4.

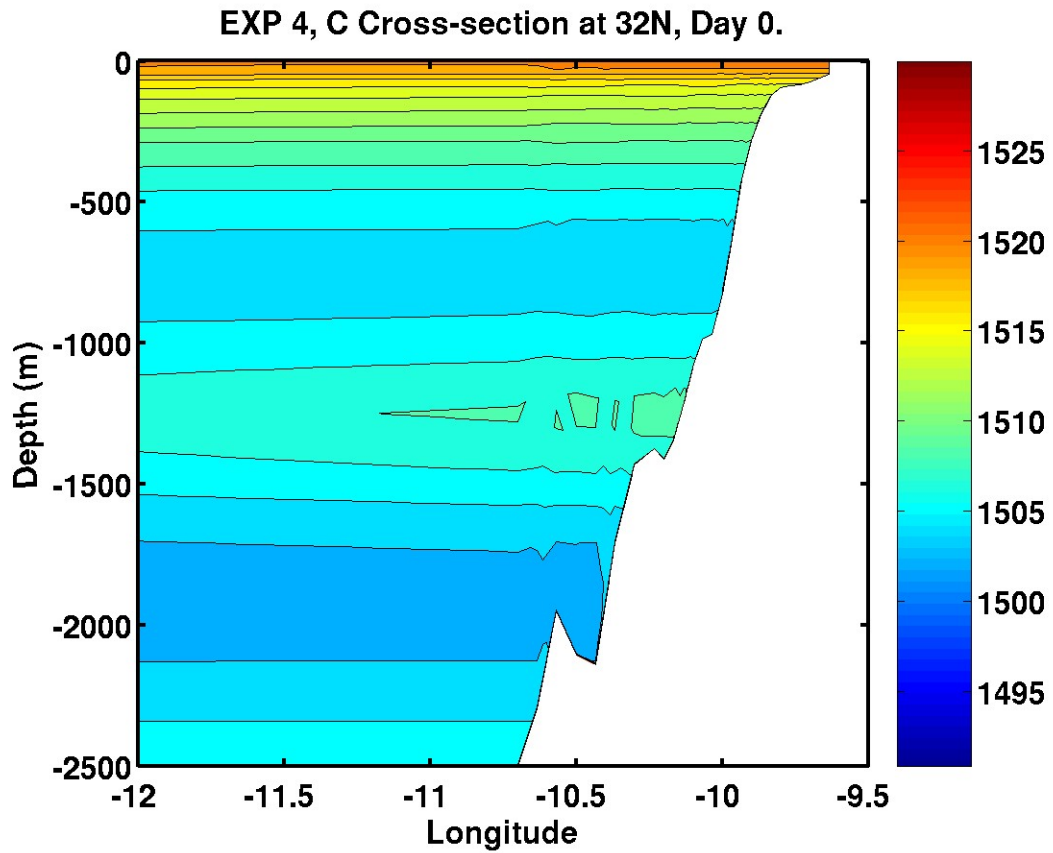Figure 13d. Sound speed (m/s) cross-section at 36°N on day 0 for Experiment 4.

Figure 13e. Sound speed (m/s) cross-section at 32°N on day
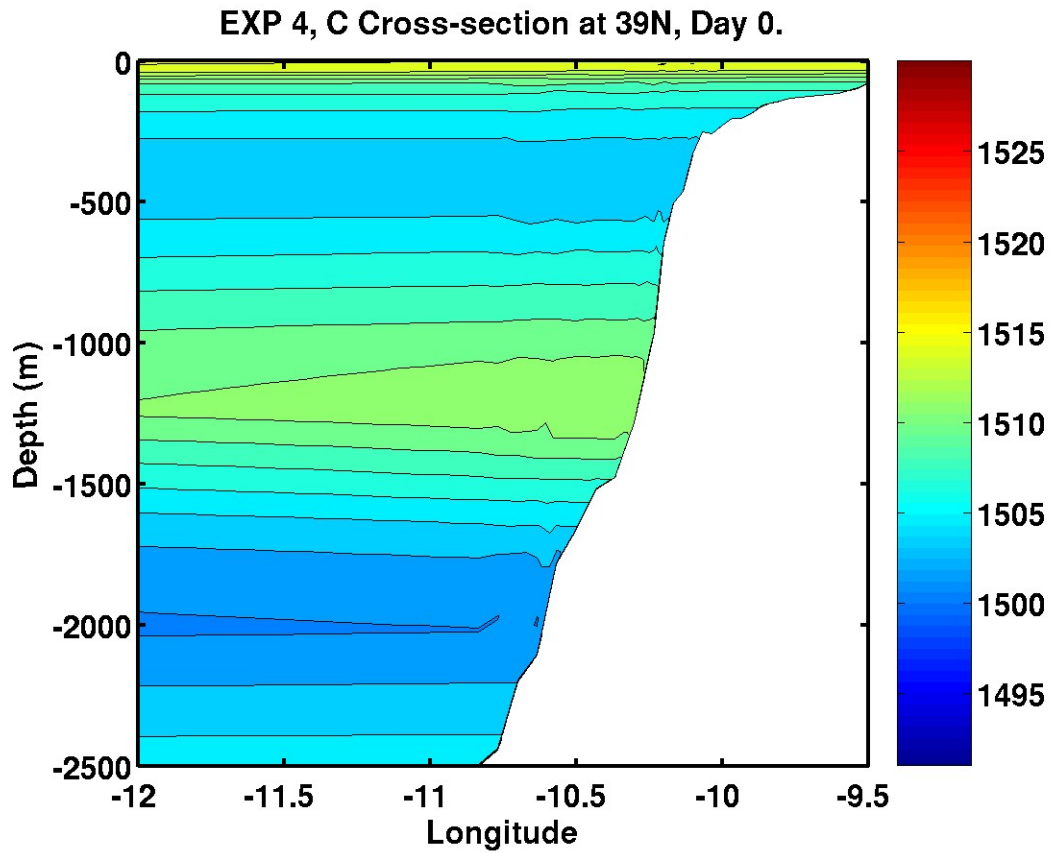0 for Experiment 4.

Figure 13f. Sound speed (m/s) cross-section at 39°N on day
0 for Experiment 4.

Figure 14a. Surface sound speed (m/s) and velocity vectors
(cm/s) on day 75 for Experiment 4.

Figure 14b. Temperature (°C) cross-section at 33.5°N on day 75 for Experiment 4.

Figure 14c. Sound speed (m/s) cross-section at 33.5°N on day 75 for Experiment 4.

EXP 4, Delta C Cross-section at 33.5N, Day75.

Figure 14d. Difference in sound speed (m/s) from initial conditions, cross-section at 33.5°N on day 75 for Experiment 4.
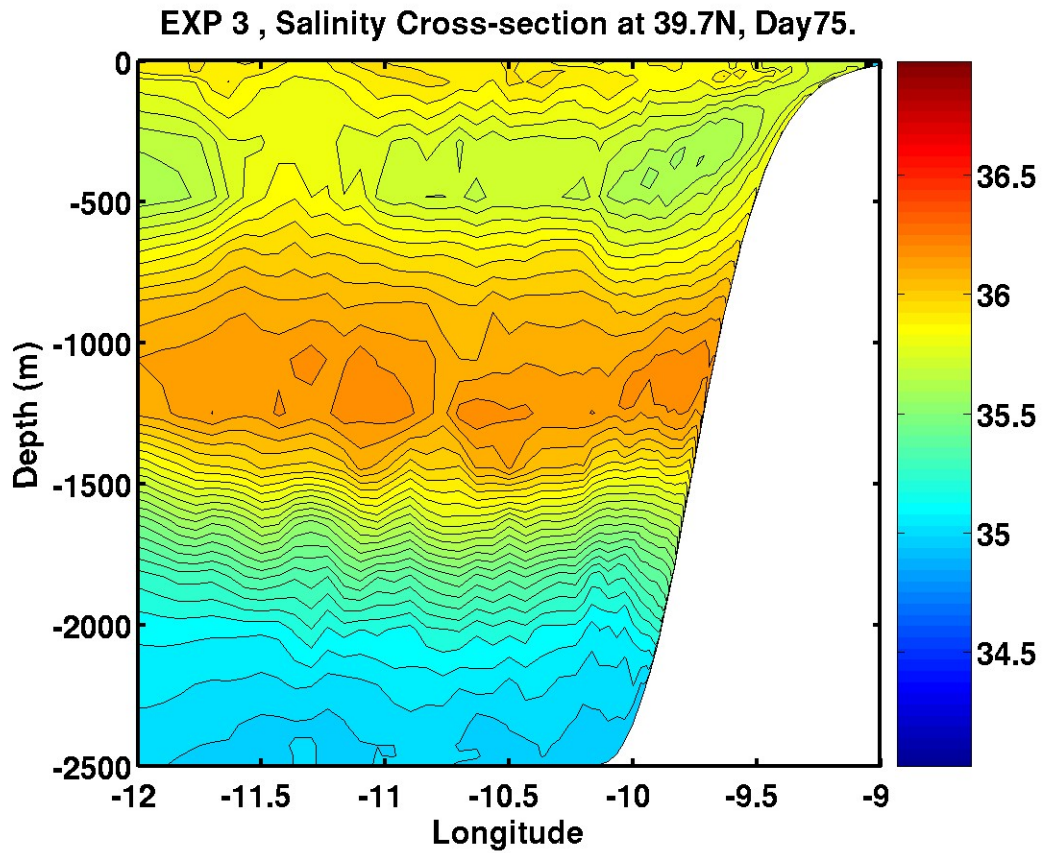
Figure 15a. Salinity (psu) cross-section at 39.7°N on day 75 for Experiment 3.
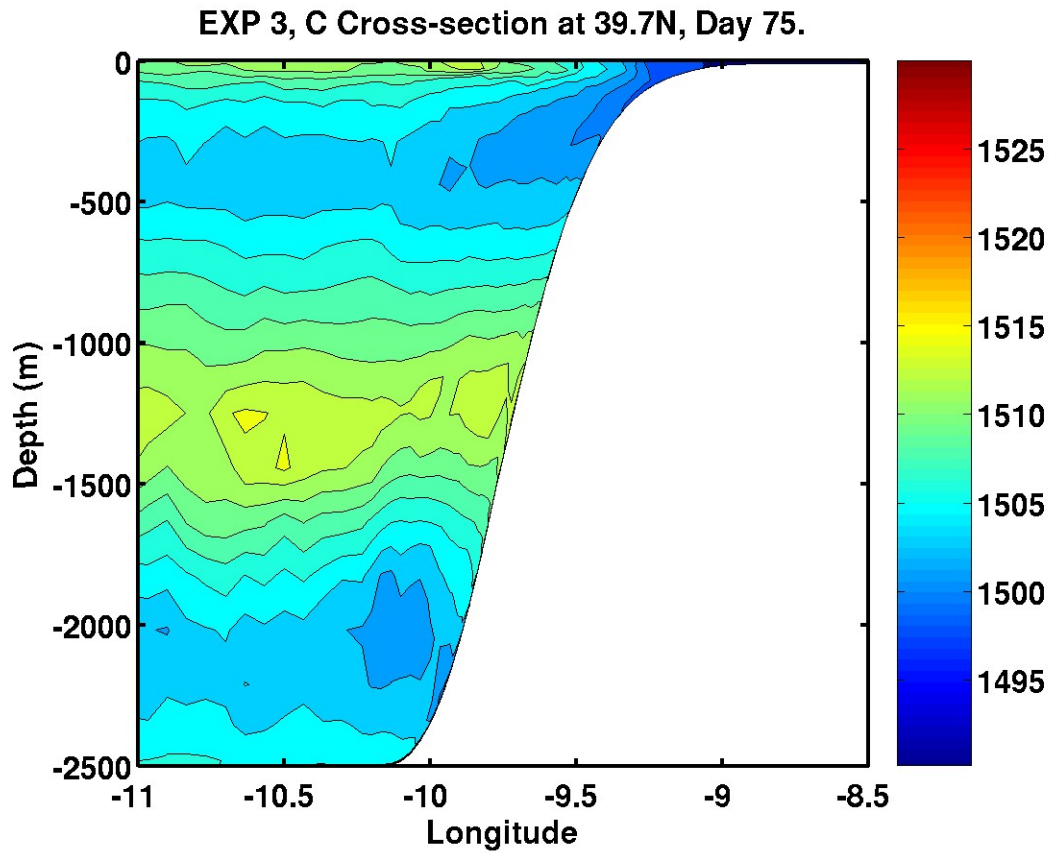
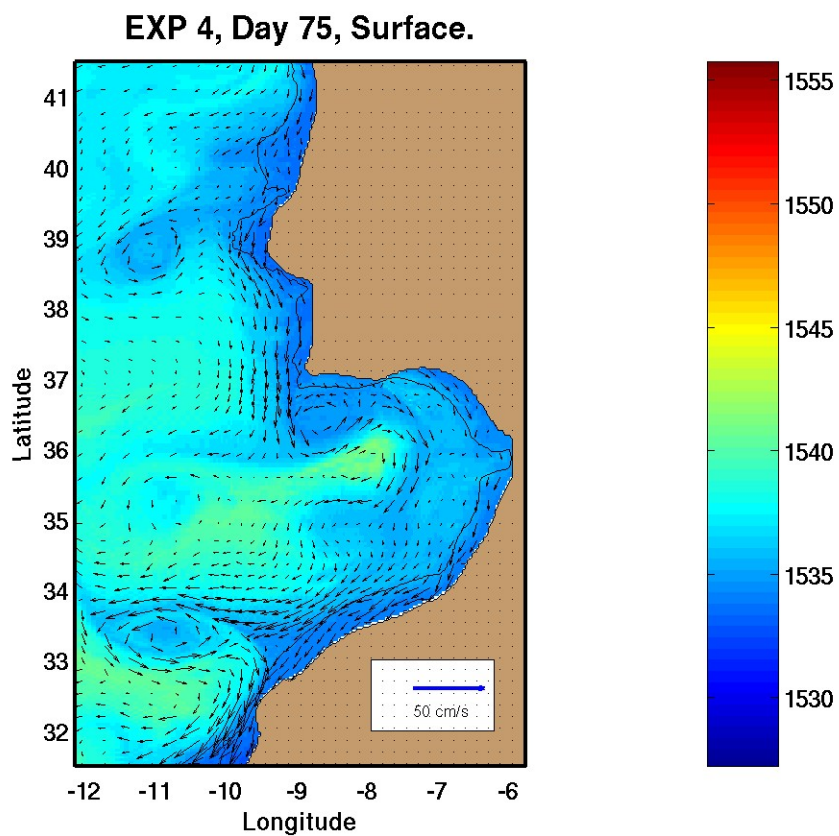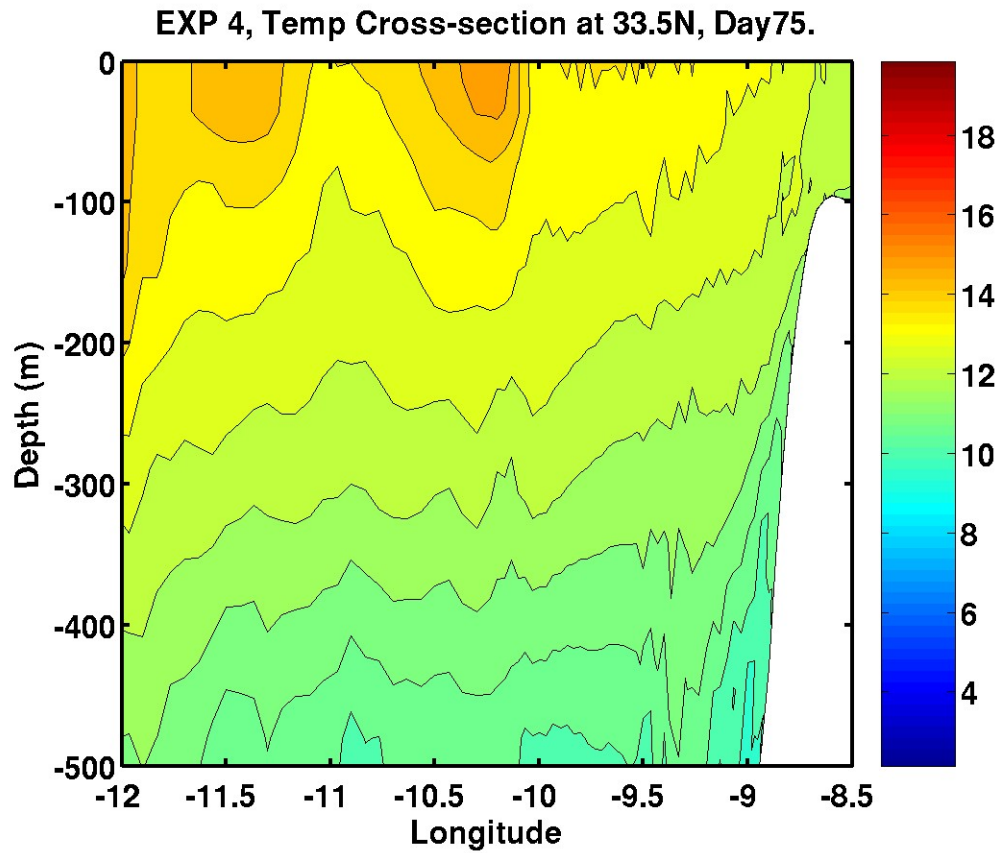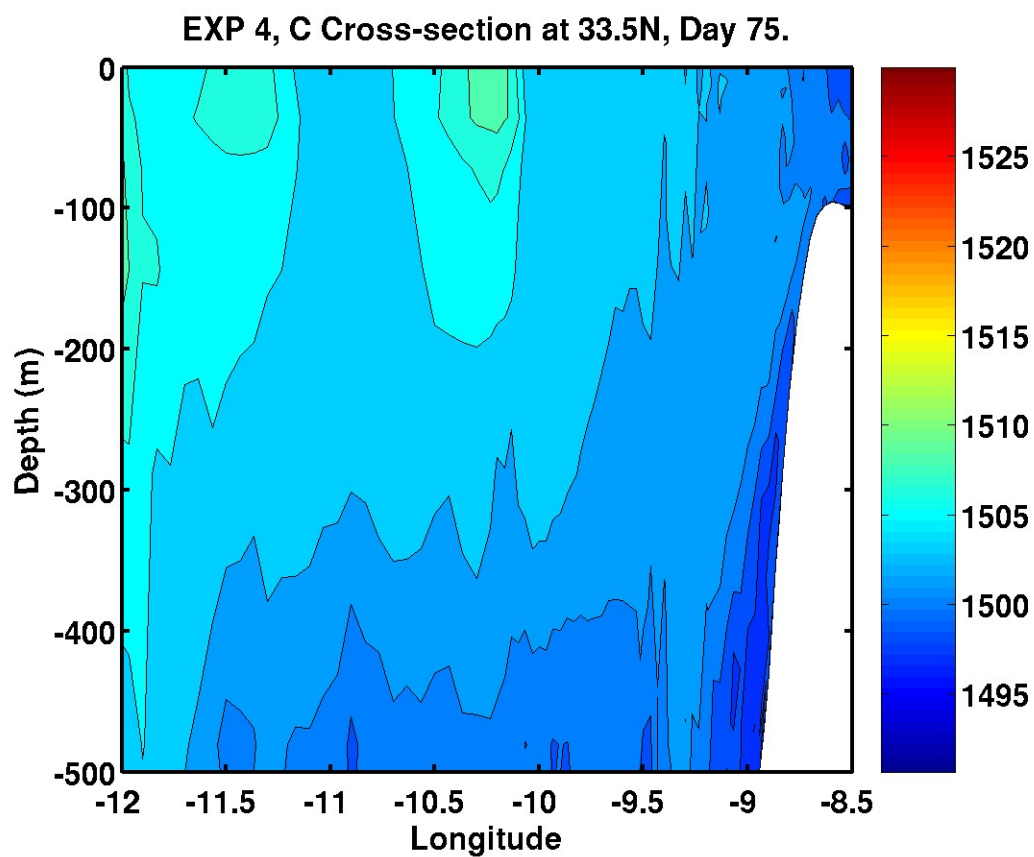Figure 15b. Sound speed (m/s) cross-section at 39.7°N on day 75 for Experiment 3.

Figure 15c. Difference in sound speed (m/s) from initial conditions, cross-section at 39.7°N on day 75 for Experiment 3.

Figure 15d. Salinity (psu) and velocity vectors (cm/s) at 1250 m depth on day 75 for Experiment 3.
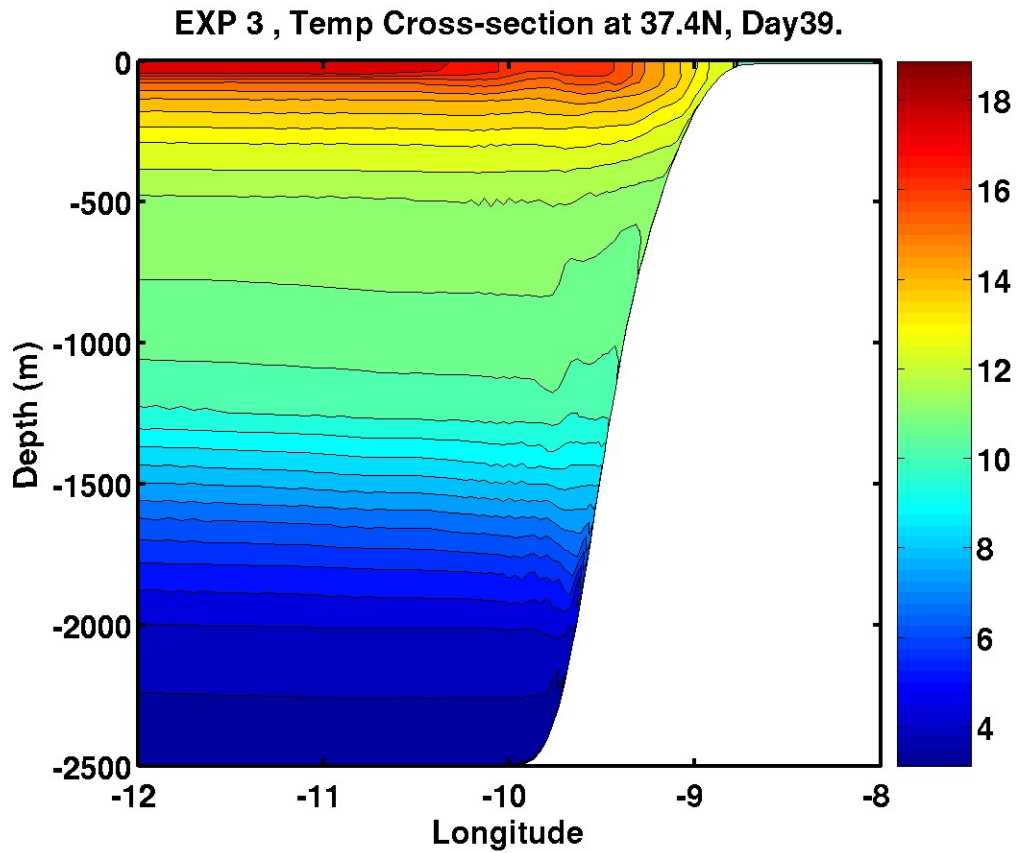
Figure 16a. Temperature (°C) cross-section at 37.4°N on day
39 for Experiment 3.

EXP 3, Delta C Cross-section at 37.4N, Day39.
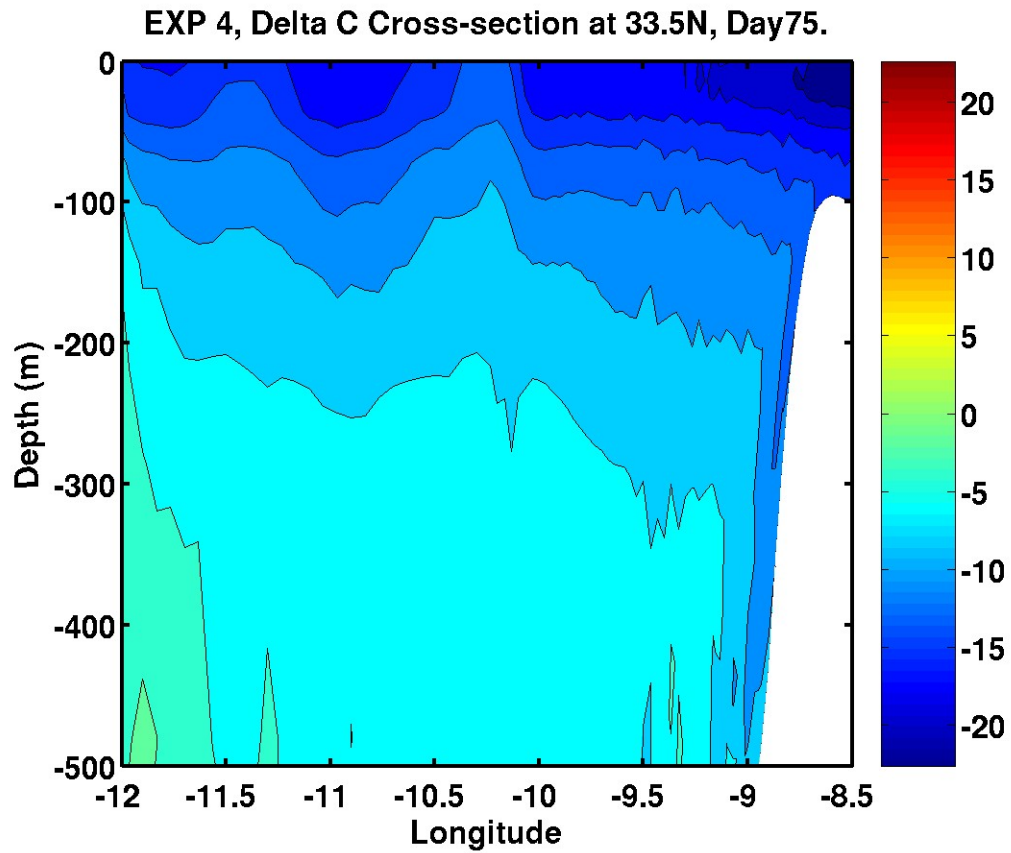
Figure 16b. Difference in sound speed (m/s) from initial conditions, cross-section at 37.4°N on day 39 for Experiment 3.
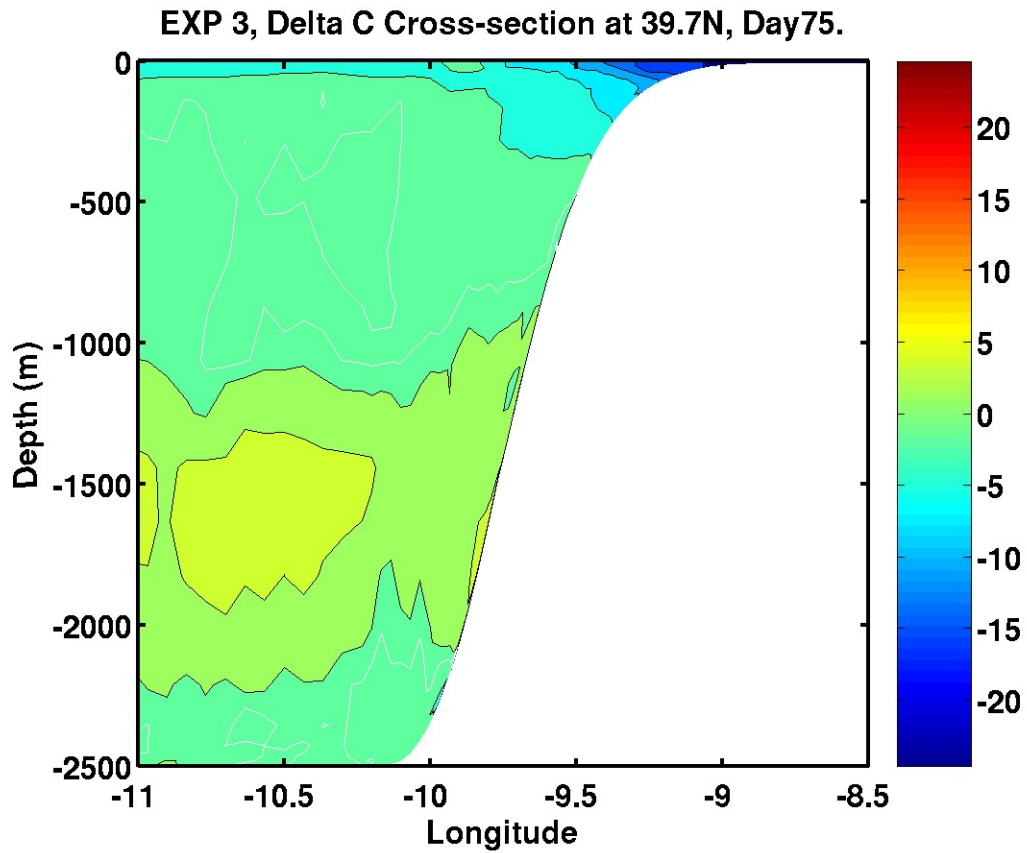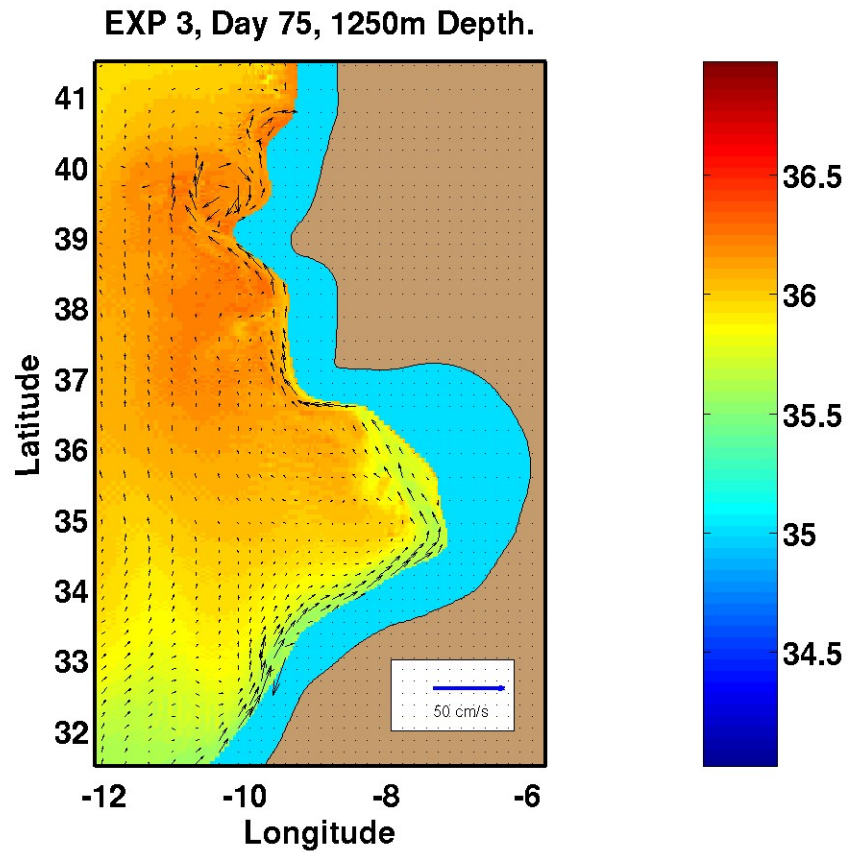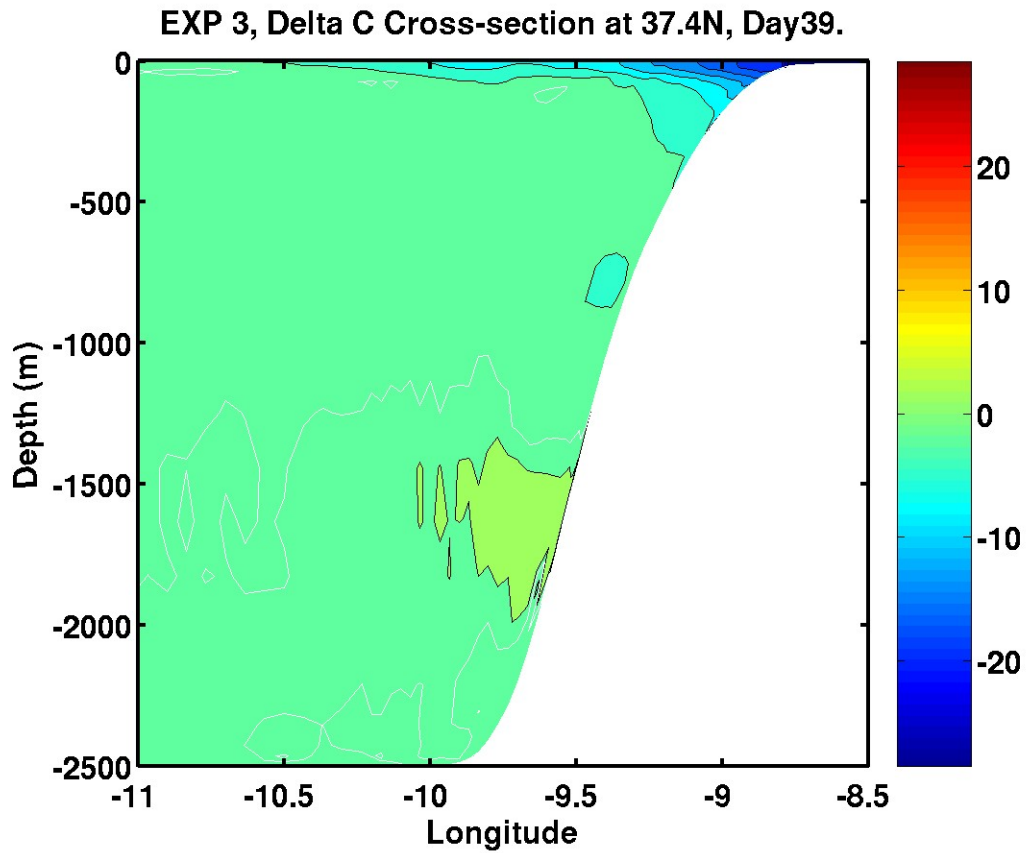
THIS PAGE INTENTIONALLY LEFT BLANK

LIST OF REFERENCES

Ambar, I., A Shallow Core of Mediterranean Water off Western Portugal, *Deep-Sea Res.*, 30, 6A, 677-680, 1983.

Ambar, I. and M.R. Howe. Observations of the Mediterranean Outflow – 1. Mixing in the Mediterranean Outflow. *Deep-Sea Res*., 26, 535-554, 1979.

Armi, L., D. Hebert, N. Oakey., J. F. Price, P. L. Richarson, H. T. Rossby, and B. Ruddick, Two Years in the Life of Mediterranean Salt Lens, *J. Phys. Oceanography*, 19, 354-370, 1989.

Barton, E.D., Eastern Boundary of the North Atlantic: Northwest Africa and Iberia. *The Sea, Vol. 11, The Global Coastal Ocean: Regional Studies and Syntheses*, K.H. Brink and A.R. Robinson, eds., Wiley, New York, Chap.22, 633-657,1998.

Batteen, M.L, J.R. Martinez, D.W. Bryan, and E.J. Buch, A modeling Study of the Coastal Eastern Boundary Current System off Iberia and Morocco, *Journal of Geophysical Research*, 105 (C6), 14,173-14,195, 2000.

Batteen, M.L, A. S. Martinho, H. A. Miller, and J. L. McClean, A Process Oriented Study of the Coastal Northern Canary Current System, *Ocean Modelling*, submitted 2006.

Blumberg, A. F., and G. L. Mellor, A Description of a Three-Dimensional Coastal Ocean Circulation Model, In: *Three-Dimensional Coastal Ocean Models, Coastal Estuarine Sci*., 4, edited by N. Heaps, 1-16, AGU, Washington, DC, 1987.

Bower, A., L. Armi, and I. Ambar, Lagrangian Observations of Meddy Formation During A Mediterranean Undercurrent Seeding Experiment, *J. Phys. Oceanography*, 27, 2545-2575, 1997.

Chapman, D. C., Numerical Treatment of Cross-Shelf Open Boundaries in a Barotropic Coastal Ocean Model, *Journal of Phys. Oceanography*, 25, 1060-1075, 1985.

Chen, C. T. and F. J. Millero, Speed of Sound in Seawater at High Pressures. *J. Acoust. Soc. Am.*, 32(10), 1357, 1977.

Coelho, H.S., Neves, R.J.J, White, M., Leitao, P.C., and A.J. Sontos, A model for ocean circulation on the Iberian Coast, *Journal of Marine Systems*, 32, 153-179, 2002.

Del Grosso, V. A., New equation for the speed of sound in natural waters (with comparisons to other equations), *J. Acoust. Soc. Am.*, 56(4), 1084-1091, 1974.

Dushaw, B. D., P. F. Worcester, B. D. Cornuelle, and B. M. Howe. On equations for the speed of sound in seawater. *J. Acoust. Soc. Am.,* 93, 255-275, 1993.

Ezer, T. and G. L. Mellor, Diagnostic and Prognostic Calculations of the North Atlantic Circulation and Sea Level Using a Sigma Coordinate Ocean Model, *J. of Geophys. Res.*, 99(C7), 14159-14171, 1994.

Ezer, T. and G. L. Mellor, Simulations of the Atlantic Ocean With a Free Surface Sigma Coordinate Ocean Model, *J. of Geophys. Res.*, 102(C7), 15647-15657, 1997.

Fofonoff, P. and R. C. Millard, Algorithms for Computation of Fundamental Properties of Seawater, *Unesco Tech. Pap. In Mar. Sci.*, 44, 53, 1983.

Frouin, R., A. F. G. Fiuza, I. Ambar, and T. J. Boyd, Observations of a Poleward Surface Current off the Coasts of Portugal and Spain during Winter, *J. Geophys. Res.*, 95, 679-691, 1990.

Fiuza, A.R. de G., The Portuguese Coastal Upwelling System, *Actual problems of Oceanography in Portugal, Junta Nacional de Investigacao Cientifica e Tecnologica, Lisboa*, 45-71, 1980.

Fiuza, A.F de G. and F.M. Sousa, Preliminary Results of a CTD Survey in the Coastal Transition Zone off Portugal During 1-9 September 1988, *Coastal Transition Zone Newsletter*, 4, 2-9 1989.

Guthrie, V. M, Dynamics of Eastern Boundary Currents and their Effect on Sound Speed Structure, Masters Thesis, Naval Postgraduate School, Monterey, CA, 91 pp, 2006.

Hagen, E., C. Zulicke, and R. Feistel, Near-Surface Structures in the Cape Ghir Filament off Morocco, *Oceanol. Acta*, 19, 6, 577-598, 1996.

Haynes, R. and E. D. Barton, A Poleward Flow Along the Atlantic Coast of the Iberian Peninsula, *J. Geophys. Res*., 95, 11425-11441, 1990.

Haynes, R., E. D. Barton, and I. Pilling, Development, Persistence and Variability of Upwelling Filaments off the Atlantic Coast of Iberia, *J. Geophys. Res.*, 98, 22681-22692, 1993.

Hebert, D., N. Oakey, and B. Ruddick, Evolution of a Mediterranean Salt Lens: Scalar Properties, *J. Phys. Oceanography*, 20, 1468-1483, 1990.

Iorga, M.C. and M.S. Lozier, Signatures of Mediterranean Outflow from a North Atlantic Climatology, 1. Salinity and Density Fields, *J. Geophys. Res*, 104, 25985-26009, 1999.

Levitus, S., and T. P. Boyer, World Ocean Atlas 1994, Vol. 4: Temperature, *NOAA Atlas NESDI 4*, 117 pp., U. S. Dept. of Commerce, Washington, D.C., 1994.

Levitus, S., R. Burgett, and T. P. Boyer, World Ocean Atlas 1994, Vol. 3: Salinity, *NOAA Atlas NESDI 3*, 99 pp., U. S. Dept. of Commerce, Washington, D.C., 1994.

Luo, Y., Guan, C., and W. Dexing, An Eta-Coordinate Version of the Princeton Ocean Model, *J. Oceanography*, 58, 589-597, 2002.

Lurton, X., *An introduction to Underwater Acoustics*, Springer: Chichester, 2002.

Marchesiello, P., J. C. McWilliams, and A. Shchepetkin, Open Boundary Conditions for Long-Term Integration of Regional Oceanic Models, *Ocean Modeling*, 3, 1-20, 2001.

Martinho, A. C., A Fine Resolution Model of the Coastal Eastern Boundary Current Systems off Iberia and Morocco, Masters Thesis, Naval Postgraduate School, Monterey, CA, 93 pp, 2001.

Martinho, A. C., and M. L.Batteen, On Reducing the Slope Parameter in Terrain-Following Numerical Ocean Models, *Ocean Modeling*, 13, 166-175, 2006.

Mellor, G. L., User's guide for a Three-Dimensional, Primitive Equation, Numerical Ocean Model, 40 pp, Program in Atmos. And Ocean Sci. Report, Princeton Univ., Princeton, NJ 1996.

Mellor, G. L., User's guide for a Three-Dimensional, Primitive Equation, Numerical Ocean Model, 40 pp, Program in Atmos. And Ocean Sci. Report, Princeton Univ., Princeton, NJ 2004.

Mellor, G. L., L. Y. Oey, and T. Ezer, Sigma Coordinate Pressure Gradient Errors and the Seamount Problem, *J. Atmospheric and Ocean Technology*, 15, 1122-1131, 1998.

Mellor, G. L., and T. Yamada, Development of a Turbulence Closure Model for Geophysical Fluid Problems, *Rev. Geophys. Space Phys*., 20, 851-875, 1982.

Palma, E. D., and R. P. Matano, On the Implementation of Passive Open Boundary Conditions for a General Circulation Model: the Barotropic Mode, *J. Geophys. Res.*, 103(C1), 1319-1341, 1998.

———, On the Implementation of Passive Open Boundary Conditions for a General Circulation Model: the Three-Dimensional Case, *J. Geophys. Res.*, 105(C4), 8605-8627, 2000.

Parrish, R. H., A. Bakun, D. M. Husby, and C. S. Nelson, Comparitive Climatology of Selected Environmental Processes in Relation to Eastern Boundary Current Pelagic Fish Reproduction, 731-778, 1983. In: *Proc. Expert Consultation to Examine Changes in Abundance and Species of Neritic Fish Resources*, FAO Fish, 291(3).

Price, J.F., and M.O. Baringer, Outflows and Deep-water Production by Marginal Seas, *Prog. Oceanogr*., 33, 161-200, 1994.

Richardson, P. L., and A. Tychensky, Meddy trajectories in the Canary Basin measured during the SEMAPHORE experiment, 1993-1995. *J. Geophys. Res.*, 103, 25029-25045, 1998.

Sandwell, D. T., and W. F. Smith, Global Bathymetric Prediction for Ocean Modeling and Marine Geophysics, 1996.

Smagorinsky, J., Manabe, S., and J. L. Holloway, Numerical Results From a Nine-Level General Circulation Model of the Atmosphere, *Mon. Weather Rev.,* 93, 727-768, 1965.

Stammer, D., H. H. Hinrichsen, and R. H. Kase, Can Meddies Be Detected By Satellited Altimetry?, *J. Geophys. Res.,* 96, 1005-7014, 1991.

Trenberth, K. E., W. G. Large, J. G. Olsen, The Mean Annual Cycle in Global Ocean Wind Stress, *J. Phys. Oceanography*, 20, 1742-1760, 1990.

Van Camp, L., L. Nykjaer, E. Mittelstaedt, and P. Schlittenhardt, Upwelling and Boundary Circulation off Northwest Africa as Depicted by Infrared and Visible Satellite Observations, *Prog. Oceanog.*, 26, 357-402, 1991.

Wilson W D, Equation for the Speed of Sound in Seawater. *J Acoust Soc Am*, 32(10), 1357, 1960.

Wooster, W. S., and J. L. Reid Jr., Eastern boundary currents, in *The Seas*, Vol. 2, edited by M. N. Hill, 253-280, John Wiley, New York, 1963.

THIS PAGE INTENTIONALLY LEFT BLANK

INITIAL DISTRIBUTION LIST

1. Defense Technical Information Center
    Ft. Belvoir, Virginia

2. Dudley Knox Library
    Naval Postgraduate School
    Monterey, California

3. Chair, Department of Oceanography (Code OC/Bv)
    Naval Postgraduate School
    Monterey, California

4. Dr. Mary L. Batteen (Code OC/Bv)
    Naval Postgraduate School
    Monterey, California

5. Dr. John A. Colosi
    Naval Postgraduate School
    Monterey, California

6. LT Alicia Hopkins
    Naval Postgraduate School
    Monterey, California

7. CDR Tony Miller
    Naval Postgraduate School
    Monterey, California